

Simulation of Second-Mode Instability in a Real-Gas Hypersonic Flow with Graphite Ablation

Clifton H. Mortensen* and Xiaolin Zhong†
University of California, Los Angeles, California 90049

DOI: 10.2514/1.J052659

A new high-order shock-fitting method with thermochemical nonequilibrium and finite-rate chemistry boundary conditions for graphite ablation is presented. The method is suitable for direct numerical simulation of boundary-layer transition in a hypersonic real-gas flow with graphite ablation. The new method is validated by comparison with three computational datasets and one set of experimental data. Direct numerical simulations were run for a 7 deg half-angle blunt cone at Mach 15.99 to find how graphite ablation and thermochemical nonequilibrium affect boundary-layer receptivity and instability. The real-gas simulation is compared with ideal-gas simulations that set their wall temperature and wall blowing from the real-gas simulation. Weak planar fast-acoustic waves in the freestream are used to perturb the steady base flow. A 525 kHz second-mode wave was found to be significantly unstable for the real-gas simulation, whereas in the ideal-gas simulations, no significant flow instability was seen. For the specific flow conditions tested, it was found that real-gas effects significantly destabilize second-mode waves.

Nomenclature

c_r	=	phase speed, m/s
c_s	=	mass fraction of species s
D	=	diffusion coefficient, m^2/s
e	=	specific total energy, J/kg
h_o	=	stagnation enthalpy, J/kg
h_s	=	species enthalpy, J/kg
k_T	=	translation-rotation thermal conductivity, $N/(K \cdot s)$
k_V	=	vibration thermal conductivity, $N/(K \cdot s)$
M	=	Mach number
M_s	=	species molecular weight, kg/mol
\dot{m}'	=	mass flux per area, $kg/(m^2 \cdot s)$
N_s	=	number density of species s , $1/m^3$
nms	=	number of molecular species
ns	=	number of species
p	=	pressure, N/m^2
$Q_{T-v,s}$	=	species vibration energy transfer rate, J/s
R	=	universal gas constant, $8.3143 J/(mol \cdot K)$
s	=	surface streamline, m
T	=	translation-rotation temperature, K
T_V	=	vibration temperature, K
u_j	=	velocity in j th direction, m/s
X_s	=	molar concentration of species s , mol/m^3
α_r	=	wave number, $1/m$
$-\alpha_i$	=	growth rate, $1/m$
ΔZ	=	perturbation amplitude of Z
ΔZ_r	=	real part of Z perturbation
δ_{ij}	=	Kronecker delta
μ	=	viscosity, $kg/(s \cdot m)$
ρ	=	density, kg/m^3
σ	=	Stefan-Boltzmann constant, $5.670 \times 10^{-8} W/(m^2 \cdot K^4)$
ω_s	=	rate of species production, $kg/(m^3 \cdot s)$

I. Introduction

ABLATING thermal protection systems are commonly used to protect hypersonic vehicles from the harsh aerothermal environment they operate in [1]. Examples include ablative heat shields for hypersonic entry vehicles, throat liners inside rocket engines, and nosetips or fins for thermal protection of hypersonic missiles. The design of these thermal protection systems is of major concern to the vehicle designer who must ensure the structural integrity of the vehicle throughout its flight envelope. For example, the Passive Nostip Technology (PANT) [2] program was designed to evaluate carbon-based nosetips for entry vehicles. They highlighted some of the design difficulties encountered when carbon nosetips are used for thermal protection, which included laminar-turbulent transition. Also, [3] highlighted some design concerns for entry vehicles due to uncertainty in hypersonic boundary-layer transition on a cone frustum, which include vehicle aerodynamics and impact dispersion. The design of thermal protection systems is an iterative process requiring the evaluation of many configurations in order to determine the optimal. Experimental testing of the various designs can be done in the laboratory or by flight tests. However, the laboratory simulation of all required hypersonic flow conditions may not be possible. Likewise, flight tests are expensive and time consuming. Thus, numerical simulations today are assuming an increasingly important role as a cost-effective complement to laboratory and flight-test research.

Practical methods for ablation prediction employ various levels of simplification, ranging from empirical engineering correlation and approximate semiempirical integral methods to very detailed full Navier-Stokes simulation methods that model the nonequilibrium, chemically reacting, fluid dynamics coupled to in-depth heat conduction material models [4–9]. Surface chemistry models are commonly used in full Navier-Stokes simulations to more accurately model surface species concentrations and mass blowing rates. Some common surface chemistry models are that of Zhukov and Abe [10] and Park [11,12].

An added design difficulty to ablation prediction is prediction of boundary-layer transition. Boundary-layer transition has a strong effect on the estimation of heating rates for Earth reentry and hypersonic vehicles. A turbulent boundary layer has a much higher heating rate than a corresponding laminar boundary layer. In turn, the heating rates impact the design of a vehicle's thermal protection system, which has a strong impact on the overall weight and cost of the vehicle. Laminar-turbulent transition in hypersonic boundary layers is a complex phenomenon involving multiple factors such as freestream disturbances, receptivity, linear eigenmode growth, and multiple paths to transition. When ablation is accounted for, there are

Presented as Paper 2012-3150 at the 42nd AIAA Fluid Dynamics Conference and Exhibit, New Orleans, LA, 25–28 June 2012; received 5 March 2013; revision received 5 March 2014; accepted for publication 6 March 2014; published online 20 June 2014. Copyright © 2014 by Clifton Mortensen and Xiaolin Zhong. Published by the American Institute of Aeronautics and Astronautics, Inc., with permission. Copies of this paper may be made for personal or internal use, on condition that the copier pay the \$10.00 per-copy fee to the Copyright Clearance Center, Inc., 222 Rosewood Drive, Danvers, MA 01923; include the code 1533-385X/14 and \$10.00 in correspondence with the CCC.

*Graduate Student, Mechanical and Aerospace Engineering; clifton.mortensen@engineering.ucla.edu. Student Member AIAA.

†Professor, Mechanical and Aerospace Engineering; xiaolin@seas.ucla.edu. Associate Fellow AIAA.

added difficulties such as shape change, ablation-induced roughness, gas influx at the surface, and thermochemical nonequilibrium.

Most research on stability of hypersonic boundary layers has been performed with a perfect-gas model, and few researchers have studied thermochemical nonequilibrium effects. Significant research on the linear stability of boundary layers has been performed by Mack [13]. Mack found that the major instability waves for hypersonic boundary layers with a perfect-gas assumption are the first and second modes. Following researchers have implemented numerical codes using linear stability theory to compute the most unstable frequencies for a variety of flow conditions and gas models. Malik [14] implemented multiple numerical methods for linear stability of perfect-gas boundary-layer flows. Stuckert and Reed [15], Hudson et al. [16], and Johnson et al. [17] studied laminar-turbulent transition in nonequilibrium, chemically reacting, hypersonic boundary layers using linear stability theory. It was found that dissociation of air species is destabilizing to the first mode and stabilizing to the second mode. Ma and Zhong [18] studied the receptivity of freestream disturbances of a Mach 10 nonequilibrium oxygen flow over a flat plate. They found that, in a Mach 10 oxygen flow, there is a significant real-gas destabilizing effect on the second-mode waves. However, they did not consider thermal nonequilibrium or any gas-surface interaction. Prakash et al. [19] studied receptivity of freestream disturbances with a thermochemical nonequilibrium shock-fitting method. Parsons et al. [20] studied the receptivity effects of thermochemical nonequilibrium on blunt cones. They found that freestream acoustic waves had higher-pressure perturbation amplitudes for a flow with thermochemical nonequilibrium than a perfect gas.

Currently, there has been a limited amount of numerical research on how ablation and surface chemistry models effect hypersonic boundary-layer transition. Johnson et al. [21] used linear stability theory to analyze nonreacting and reacting hypersonic boundary-layer stabilities with blowing and suction. Ghaffari et al. [22] performed a linear stability analysis of a hypersonic perfect-gas flat-plate boundary layer with wall blowing and found that, as blowing increases, the maximum amplification rate of the disturbance instability grows and moves to lower frequencies. Li et al. [23] studied boundary-layer instability mechanisms for hypersonic perfect-gas flows over slender cones and blunt capsules at a zero angle of attack and an angle of attack of 16 deg. They found that outgassing is moderately stabilizing to the second mode for the slender cone and is destabilizing to the first mode for the blunt capsule.

The goal of this paper is twofold: 1) to develop and validate a new high-order shock-fitting method for hypersonic flows with thermochemical nonequilibrium and finite-rate boundary conditions for graphite surface ablation, and 2) to perform an initial investigation of hypersonic boundary-layer disturbances in the presence of real-gas effects and graphite ablation effects using the developed direct numerical simulation (DNS) method. While there are many combinations of gas phase models and surface chemistry models for thermochemical nonequilibrium and graphite ablation, the particular combination of models used here is similar to those used in [4], with some modifications. An 11-species gas model is used to model chemical nonequilibrium. It contains a standard five-species air model (N_2 , O_2 , NO , N , and O) without ionization. The remaining species (C_3 , CO_2 , C_2 , CO , CN , and C) are obtained from sublimation, oxidation, and reactions of ablation products with five-species air. A two-temperature model is used to simulate thermal nonequilibrium. The surface reactions considered contain oxidation, recombination of atomic oxygen, and sublimation. A surface mass balance is used to set species mass fractions at the surface, and temperature profiles within the ablator are not computed.

Whereas current thermal protection materials have advanced beyond graphite, many are still carbon based. Thus, graphite ablation provides a good baseline test case where results can be extrapolated to other carbon-based ablators such as NASA's phenolic impregnated carbon ablator (PICA). In [6], PICA is modeled similar to graphite with the inclusion of an extra term in the surface mass balance and a more complex gas phase model due to hydrogen entering the

freestream from pyrolysis gas injection. Surface recession and ablation-induced roughness due to the graphitic ablator are not included in the current simulations. For the configuration studied here, the surface recession rate is low. This low rate will most likely have a minimal impact on second-mode waves, which have a high frequency commonly in hundreds of kilohertz. Unlike surface recession rates, ablation-induced roughness likely has a large impact on transition. To date, the effect of surface roughness on hypersonic boundary-layer transition is an open research problem in itself. Thus, it was decided to concentrate on first trying to understand ablative effects due to a real gas interacting with a graphite surface in the absence of ablation-induced roughness. The logical next step would be to include the effects of ablation-induced roughness.

The DNS geometry for the receptivity study was chosen as a generic configuration for slender hypersonic vehicles or entry vehicles with ablative nosetips and/or aeroshells. This was done to study the fundamental physics underlying boundary-layer transition for slender geometries at zero incidence, which are commonly second-mode dominated rather than study transition on a specific vehicle.

The paper will start with an overview of the governing equations and gas phase models followed by an overview of the numerical method and surface chemistry model, after which the shock-fitting scheme with the implemented models will be validated with cases computed by [4] and compared to a graphite ablation case computed in [6] with corresponding experimental data. After code validation, a DNS is run of a 7 deg half-angle blunt cone at Mach 15.99 to study hypersonic boundary-layer receptivity and instability in the presence of graphite ablation and thermochemical nonequilibrium.

II. Governing Equations and Gas Phase Models

The governing equations for thermochemical nonequilibrium are formulated for a two-temperature model, with the rotational energy mode assumed to be fully excited and 11 nonionizing species with finite-rate chemistry. Two temperatures are used to represent translation-rotation energy and vibration energy. The 11-species model (N_2 , O_2 , NO , C_3 , CO_2 , C_2 , CO , CN , N , O , and C) is used to simulate air, surface reactions, and reactions of air with ablation products. The conservative three-dimensional Navier-Stokes equations consist of 11-species mass conservation equations, three momentum conservation equations, the vibration energy conservation equation, and the total energy conservation equation. Wang and Zhong [24] and Prakash et al. [25] have used similar formulations for shock-fitting DNS of thermochemical nonequilibrium flow. Written in vector form, the governing equations are

$$\frac{\partial \mathbf{U}}{\partial t} + \frac{\partial F_j}{\partial x_j} + \frac{\partial G_j}{\partial x_j} = \mathbf{W} \quad (1)$$

where \mathbf{U} is the state vector of conserved quantities, and \mathbf{W} are the source terms defined by

$$\mathbf{U} = \begin{bmatrix} \rho_1 \\ \vdots \\ \rho_{ns} \\ \rho u_1 \\ \rho u_2 \\ \rho u_3 \\ \rho e \\ \rho e_v \end{bmatrix}, \quad \mathbf{W} = \begin{bmatrix} \omega_1 \\ \vdots \\ \omega_{ns} \\ 0 \\ 0 \\ 0 \\ 0 \\ \sum_{s=1}^{nms} (Q_{T-v,s} + \omega_s e_{v,s}) \end{bmatrix}$$

F_j and G_j are the inviscid and viscous fluxes, respectively, and are defined by

$$F_j = \begin{bmatrix} \rho_1 u_j \\ \vdots \\ \rho_{ns} u_j \\ \rho u_1 u_j + p \delta_{1j} \\ \rho u_2 u_j + p \delta_{2j} \\ \rho u_3 u_j + p \delta_{3j} \\ (\rho e + p) u_j \\ \rho e_v u_j \end{bmatrix}, \quad G_j = \begin{bmatrix} \rho_1 v_{1j} \\ \vdots \\ \rho_{ns} v_{nsj} \\ \tau_{1j} \\ \tau_{2j} \\ \tau_{3j} \\ -u_i \tau_{ij} - k_T \frac{\partial T}{\partial x_j} - k_V \frac{\partial T_v}{\partial x_j} + \sum_{s=1}^{nms} \rho_s h_s v_{sj} \\ -k_V \frac{\partial T_v}{\partial x_j} + \sum_{s=1}^{nms} \rho_s e_{v,s} v_{sj} \end{bmatrix}$$

where v_{sj} is the species diffusion velocity, and

$$\tau_{ij} = \mu \left(\frac{\partial u_i}{\partial x_j} + \frac{\partial u_j}{\partial x_i} \right) - \frac{2}{3} \mu \frac{\partial u_k}{\partial x_k} \delta_{ij}$$

is the viscous stress. The total energy per unit volume ρe is defined by

$$\rho e = \sum_{s=1}^{ns} \rho_s c_{v,s} T + \rho e_v + \frac{1}{2} \rho u_i u_i + \sum_{s=1}^{ns} \rho_s h_s^o \quad (2)$$

where h_s^o is the heat of formation of species s , $e_{v,s}$ is the species-specific vibration energy, and $c_{v,s}$ is the species translation-rotation specific heat at constant volume defined as

$$c_{v,s} = \begin{cases} \frac{5}{2} \frac{R}{M_s}, & s = 1, 2, \dots, nms \\ \frac{3}{2} \frac{R}{M_s}, & s = nms + 1, \dots, ns \end{cases} \quad (3)$$

The vibration energy per unit volume ρe_v is defined as

$$\rho e_v = \sum_{s=1}^{nms} \rho_s e_{v,s} = \sum_{s=1}^{nms} \rho_s \left(\sum_{m=1}^{nmod} \frac{g_{s,m} R}{M_s} \frac{\theta_{v,s,m}}{\exp(\theta_{v,s,m}/T_v) - 1} \right) \quad (4)$$

where $nmod$ refers to the number of vibrational modes for each polyatomic molecule, $\theta_{v,s,m}$ refers to the characteristic temperature of each vibrational mode, and $g_{s,m}$ is the degeneracy of each vibrational mode. For the diatomic species, there is only one vibrational mode and the degeneracy is unity. For C_3 and CO_2 , there are three vibrational modes, where two modes have a degeneracy of unity and one has a degeneracy of two. The characteristic vibration temperatures and their degeneracies were taken from Park [26] for N_2 , O_2 , and NO ; from Dolton et al. [27] for C_3 ; and from McBride et al. [28] for CO_2 , C_2 , CO , and CN .

To model chemical nonequilibrium, 8 dissociation reactions and 16 exchange reactions are used. Each reaction is governed by a forward and backward reaction rate determined by Eqs. (5) and (6), respectively. The dissociation reactions are given in Table A1 along with their corresponding forward reaction rate constants in Arrhenius form. The exchange reactions with corresponding forward reaction rate constants are given in Table A2. All forward reaction rate constants are taken from [29–31]. T_a is the defining temperature for the reaction and is defined as $T_a = \sqrt{TT_v}$ for reactions 1–3 and as $T_a = T$ for all other reactions. When computing the backward reaction rate for all reactions, $T_a = T$:

$$k_f = C_f T_a^n \exp(-\theta_d/T_a) \quad (5)$$

$$k_b = k_f/K_{eq} \quad (6)$$

The equilibrium coefficient K_{eq} is computed in two different ways. A curve fit from Park [26] is employed for reactions 1–3 and 9–10, as in Eq. (7). The equilibrium coefficients for the remaining reactions are computed from the Gibbs free energy. Curve fits to the Gibbs free energy are obtained from McBride et al. [28], as in Eqs. (8) and (9), respectively, where Δn is the stoichiometric coefficients of the products minus the reactants:

$$K_{eq} = A_0 \exp\left(\frac{A_1}{Z} + A_2 + A_3 \ln(Z) + A_4 Z + A_5 Z^2\right), \quad Z = \frac{10,000}{T} \quad (7)$$

$$\frac{G^o}{RT} = a_1(1 - \ln T) - \frac{a_2}{2} T - \frac{a_3}{6} T^2 - \frac{a_4}{12} T^3 - \frac{a_5}{20} T^4 + \frac{a_6}{T} - a_7 \quad (8)$$

$$K_{eq} = \exp\left(-\frac{G^o}{RT}\right) (R_u T)^{-\Delta n} \quad (9)$$

To calculate the source term in the vibration energy equation that represents the exchange of energy between the translation-rotation and vibration energies, the Landau–Teller expression is used:

$$Q_{T-v,s} = \rho_s \frac{e_{v,s}(T) - e_{v,s}(T_v)}{\langle \tau_s \rangle + \tau_{cs}} \quad (10)$$

where $\langle \tau_s \rangle$ is the Landau–Teller vibration relaxation time given by Lee [32] and defined as

$$\langle \tau_s \rangle = \frac{\sum_{r=1}^{ns} X_r}{\sum_{r=1}^{ns} X_r / \tau_{sr}} \quad (11)$$

and τ_{sr} is obtained from Millikan and White [33] using

$$\tau_{sr} = \frac{1}{p} \exp[A_{sr}(T^{-1/3} - 0.015\mu_{sr}^{1/4}) - 18.42], \quad p \text{ atm} \quad (12)$$

$$A_{sr} = 1.16 \times 10^{-3} \mu_{sr}^{1/2} \theta_{v,s}^{4/3} \quad (13)$$

$$\mu_{sr} = \frac{M_s M_r}{M_s + M_r} \cdot 1000 \quad (14)$$

Here, $\theta_{v,s}$ is the characteristic temperature corresponding to the energy level of the first excited vibrational mode. From Park [26], τ_{cs} is used to more accurately model the relaxation time in areas of high temperatures occurring just downstream of the bow shock:

$$\tau_{cs} = 1/C_s \sigma_v N_s \quad (15)$$

$$C_s = \sqrt{8RT/\pi M_s} \quad (16)$$

$$\sigma_v = 10^{-21} (50,000/T)^2 \quad (17)$$

The viscosity of each species is computed using a Blottner curve fit, shown in Eq. (18). The coefficients are obtained from Blottner et al. [34], Gupta et al. [35], and Candler [36], and they are shown in Table A3. The mixture viscosity is then found using each species viscosity from a mixing rule obtained from Wilke [37], as shown in Eqs. (19–21):

$$\mu_s = 0.1 \exp[(A_s^\mu \ln(T) + B_s^\mu) \ln(T) + C_s^\mu] \quad (18)$$

$$\mu = \sum_{s=1}^{ns} \frac{X_s \mu_s}{\phi_s} \quad (19)$$

$$X_s = \frac{c_s}{M_s} \quad (20)$$

$$\phi_s = \frac{\sum_{r=1}^{ns} X_r [1 + (\frac{M_r}{M_s})^{1/4}]^2}{[8(1 + \frac{M_r}{M_s})]^{1/2}} \quad (21)$$

The translation-rotation and vibration heat conductivities for each species are calculated from Eqs. (22) and (23), where

$$c_{v, tr, s} = \frac{3}{2} \frac{R}{M_s} \quad c_{v, rot, s} = \frac{R}{M_s}$$

and

$$c_{v, vib, s} = \frac{\partial e_{v, s}}{\partial T_V}$$

for molecules, and they are zero otherwise. The total heat conductivities for each energy mode are combined, similar to the viscosity using Eqs. (24) and (25). The diffusion velocity is calculated using Fick's law [Eq. (26)] and a constant Schmidt number [Eq. (27)], which yields acceptable results for species with similar molecular weights:

$$k_{T, s} = \mu_s \left(\frac{5}{2} c_{v, tr, s} + c_{v, rot, s} \right) \quad (22)$$

$$k_{V, s} = \mu_s c_{v, vib, s} \quad (23)$$

$$k_T = \sum_{s=1}^{ns} \frac{X_s k_{T, s}}{\phi_s} \quad (24)$$

$$k_V = \sum_{s=1}^{ns} \frac{X_s k_{V, s}}{\phi_s} \quad (25)$$

$$\rho_s v_{sj} = -\rho D_s \frac{\partial c_s}{\partial x_j} \quad (26)$$

$$Sc = \frac{\mu}{\rho D} = 0.5 \quad (27)$$

III. Numerical Method

A high-order shock-fitting method developed for perfect-gas flow by Zhong [38] has been extended for use on thermochemical nonequilibrium flows to compute the flowfield between the shock and the body. For shock-fitting computations, the shock location is not known a priori, so its position is solved along with the flowfield. Since the shock position is not stationary, the grid used to compute the flowfield is a function of time. This leads to the coordinate transformation

$$\begin{cases} \xi = \xi(x, y, z) \\ \eta = \eta(x, y, z, t) \\ \zeta = \zeta(x, y, z) \\ \tau = t \end{cases} \Leftrightarrow \begin{cases} x = x(\xi, \eta, \zeta, \tau) \\ y = y(\xi, \eta, \zeta, \tau) \\ z = z(\xi, \eta, \zeta, \tau) \\ t = \tau \end{cases}$$

where y is normal to the body, x is in the streamwise direction, z is in the transverse direction, $\zeta_t = 0$, and $\xi_t = 0$. The governing equation can then be transformed into computational space as

$$\frac{1}{J} \frac{\partial U}{\partial \tau} + \frac{\partial E'}{\partial \xi} + \frac{\partial F'}{\partial \eta} + \frac{\partial G'}{\partial \zeta} + \frac{\partial E_{v'}}{\partial \xi} + \frac{\partial F_{v'}}{\partial \eta} + \frac{\partial G_{v'}}{\partial \zeta} + U \frac{\partial(1/J)}{\partial \tau} = \frac{W}{J} \quad (28)$$

where J is the Jacobian of the coordinate transformation, and

$$E' = \frac{F_1 \xi_x + F_2 \xi_y + F_3 \xi_z}{J} \quad (29)$$

$$F' = \frac{F_1 \eta_x + F_2 \eta_y + F_3 \eta_z}{J} \quad (30)$$

$$G' = \frac{F_1 \zeta_x + F_2 \zeta_y + F_3 \zeta_z}{J} \quad (31)$$

$$E_{v'} = \frac{G_1 \xi_x + G_2 \xi_y + G_3 \xi_z}{J} \quad (32)$$

$$F_{v'} = \frac{G_1 \eta_x + G_2 \eta_y + G_3 \eta_z}{J} \quad (33)$$

$$G_{v'} = \frac{G_1 \zeta_x + G_2 \zeta_y + G_3 \zeta_z}{J} \quad (34)$$

A seven-point stencil is used to discretize the spatial derivatives

$$\frac{df_i}{dx} = \frac{1}{hb_i} \sum_{k=-3}^3 \alpha_{i+k} f_{i+k} - \frac{\alpha}{6! b_i} h^5 \left(\frac{\partial^6 f}{\partial x^6} \right) \quad (35)$$

where

$$a_{i \pm 3} = \pm 1 + \frac{1}{12} \alpha, \quad a_{i \pm 2} = \mp 9 - \frac{1}{2} \alpha \quad (36)$$

$$a_{i \pm 1} = \pm 45 + \frac{5}{4} \alpha, \quad a_i = -\frac{5}{3} \alpha \quad (37)$$

$$b_i = 60 \quad (38)$$

and where $\alpha < 0$ is a fifth-order upwind explicit scheme and $\alpha = 0$ reduces to a sixth-order central scheme. Here, the inviscid terms use $\alpha = -6$, which yields a low-dissipation fifth-order upwind difference, and the viscous terms are discretized using $\alpha = 0$. Flux splitting is used for the inviscid flux terms, and to compute second derivatives, the first-order derivative operator is applied twice. Explicit Euler is used to advance the solution in time.

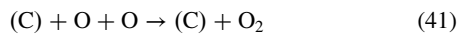
Conditions behind the shock are calculated from Rankine-Hugoniot relations. In the freestream, the flow is assumed to be in thermal equilibrium and the chemical composition of the flow is fixed. The shock is assumed to be infinitely thin, resulting in no relaxation as the flow crosses the shock, since relaxation rates are finite. This leads to the chemical composition remaining constant

across the shock as well as the vibration temperature. Since neither process has any time to relax across the shock, the relaxation zone is entirely downstream of the shock. A complete derivation of thermochemical nonequilibrium shock fitting can be found from Prakash et al. [19].

IV. Surface Chemistry Model and Boundary Conditions

The surface chemistry model accounts for reactions occurring at the graphite surface between the solid surface carbon and freestream gaseous species. Six surface reactions are taken into account: the first two reactions allow for surface removal of material through oxidation, the third reaction accounts for surface recombination of atomic oxygen, and the last three are due to sublimation of C, C₂, and C₃. C₃ is commonly included in most graphite ablation models, as sublimation of graphite produces mostly C₃ with smaller amounts of C, C₂, and heavier carbon species. Nitridation is not included here, as there is still significant uncertainty in the nitridation coefficient. There has been recent experimental work to determine the nitridation coefficient by Suzuki et al. [39] as well as Park and Bogdanoff [40]. It is likely the nitridation coefficient is small, leading to a minimal impact on the simulation when nitridation is excluded.

The reactions and reaction probabilities for oxidation and recombination of atomic oxygen are obtained from Park [12], yielding



The oxidation rates are based on kinetic theory, giving

$$k_m = \alpha_m \sqrt{\frac{RT_w}{2\pi M_s}} \quad (42)$$

where T_w is the wall temperature and α_m is the reaction probability for each reaction in Eqs. (39–41), respectively. The reaction probabilities are obtained experimentally, yielding

$$\alpha_1 = \frac{1.43 \times 10^{-3} + 0.01 \exp(-1450/T_w)}{1 + 2 \times 10^{-4} \exp(13,000/T_w)} \quad (43)$$

$$\alpha_2 = 0.63 \exp(-1160/T_w) \quad (44)$$

$$\alpha_3 = 0.63 \exp(-1160/T_w) \quad (45)$$

From which the associated surface species mass flux may be found from

$$\dot{m}'_{O_2} = -\rho_{O_2} k_1 + \rho_O k_3 \quad (46)$$

$$\dot{m}'_{CO} = \frac{M_{CO}}{M_{O_2}} \rho_{O_2} k_1 + \frac{M_{CO}}{M_O} \rho_O k_2 \quad (47)$$

$$\dot{m}'_O = \frac{M_O}{M_{O_2}} \rho_{O_2} k_1 - \rho_O k_2 - \rho_O k_3 \quad (48)$$

There are three reactions for sublimation:



and for each reaction, the mass flux is obtained from the Knudsen–Langmuir equation [41]

$$\dot{m}'_s = \alpha_s (p_{v,s} - p_s) \sqrt{\frac{M_s}{2\pi RT_w}} \quad (52)$$

where α_s is experimentally determined for each carbon species. The vapor pressure of the three carbon species is given by

$$p_{v,s} = \exp\left(\frac{P_s}{T_w} + Q_s\right) p \text{ atm} \quad (53)$$

where Table A4 gives the reaction probabilities obtained from [42] and vapor pressure coefficients obtained from [27] for each sublimation reaction.

Boundary conditions are needed to couple the surface chemistry model with the gas model as well as set wall conditions for both temperatures and pressure. At the surface, a surface energy balance is solved to find temperature and a surface mass balance is solved to find the mass fraction of each species. A simplified surface energy balance is used to avoid a complicated flow/solid coupling and allow the focus of the simulation to stay on boundary-layer stability. The surface energy balance is

$$k_T \frac{\partial T}{\partial n} + k_V \frac{\partial T_V}{\partial n} + \sum_{s=1}^{ns} \rho h_s D_s \frac{\partial c_s}{\partial n} = \sigma \epsilon T^4 + \dot{m}' \sum_{s=1}^{ns} c_s h_{s,o} \quad (54)$$

where

$$h_{s,o} = \left(c_{v,s} + \frac{R}{M_s}\right) T + e_{v,s} + h_s^o + \frac{1}{2}(u_1^2 + u_2^2 + u_3^2) \quad (55)$$

and all values and derivatives are taken at the wall. For the carbon surface, $\epsilon = 0.9$ and σ is the Stefan–Boltzmann constant. Each derivative is taken normal to the surface, where n represents the direction normal to the surface. Derivatives of fifth-order Lagrange polynomials are used to compute the normal derivatives at the surface.

The surface mass balance for each species is

$$\rho_s u_n - \rho D \frac{\partial c_s}{\partial n} = \dot{m}'_s \quad (56)$$

where each value and derivative is taken at the wall. The total mass balance found from summing Eq. (56) is

$$\rho u_n = \dot{m}' \quad (57)$$

where the total mass flux is found from the sum of each species mass flux as

$$\dot{m}' = \sum_{s=1}^{ns} \dot{m}'_s \quad (58)$$

Lastly, a condition for pressure is required at the surface. It is common to assume that $\frac{\partial p}{\partial n} = 0$ from the wall normal momentum equation for a wall with no slip. A finite velocity is obtained normal to the surface due to surface chemical reactions in ablation simulations making $\frac{\partial p}{\partial n} = 0$ invalid. Instead, the one-dimensional subsonic inlet conditions may be used as in [4]. It is also common to use pressure extrapolation at the surface, which is valid for a wall with no slip and a surface with a nonzero surface normal velocity. In the present work, fifth-order pressure extrapolation employing Lagrange polynomials

Table 1 Freestream conditions for PANT case 1

Parameter	Value
M_∞	15.99
ρ_∞	2.4093×10^{-2} kg/m ³
p_∞	2026.0 N/m ²
C_{N_2}	0.7635
C_{O_2}	0.2365

is used instead of the one-dimensional subsonic inlet approach, as extrapolation allows the high-order solution procedure for the interior points to set the wall pressure.

V. Validation

Three validation cases are computed with the shock-fitting code using the 11-species gas model and the surface chemistry model. Two cases are compared to those of the simulations in [4], and one case is compared to a simulation from [6] that has corresponding experimental data. Recall that [4] has served as a starting point for the gas model and surface chemistry model. It should be noted that [4] and [6] use shock-capturing methods, whereas a shock-fitting method is used in this work.

A. Comparison to $M_\infty = 15.99$ Simulation of PANT Case 1

The first test case freestream conditions come from experimental tests on graphite from the Passive Nostip Technology program [2] and are called PANT case 1. The experimental facility used to conduct these tests is the Arnold Engineering Development Center Aeroballistic Range G. The freestream conditions are given in Table 1. The geometry is a sphere cylinder with a nose radius of 0.635 cm. The grid was chosen similar to [4] using 32 points on the

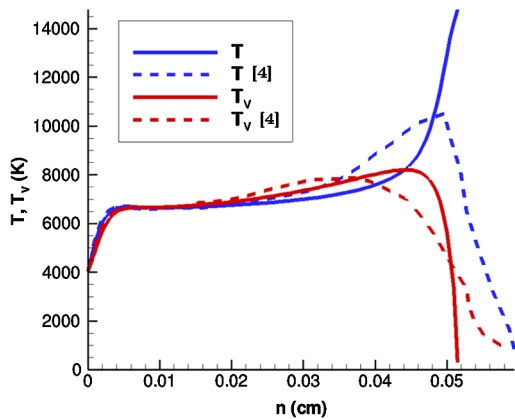


Fig. 1 Translation-rotation temperature and vibration temperature comparison on the stagnation line.

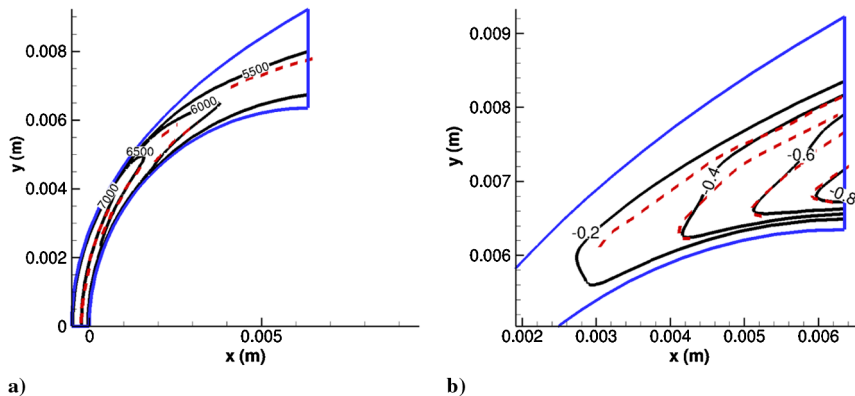


Fig. 2 Comparison of a) T_v contours, and b) $1 - T/T_v$ contours, where the dashed lines are from [4] and the black lines are from the current simulation.

surface and 91 points in the surface-normal direction. However, the shock-fitting method uses a two-sided stretching in the wall-normal direction to accurately capture relaxation processes just downstream of the shock, whereas [4] uses a one-sided boundary-layer stretching. In the shock-fitting code, there is no computation of the temperature within the graphite ablative material, but [4] does compute the temperature within the ablator. For a more reasonable comparison, a curve fit of the simulated surface temperature in [4] was used to set the two surface temperatures rather than using the surface energy balance. Only the sphere region has been computed for comparison, as this is the region where ablation effects are the most pronounced.

Figure 1 gives a comparison of the stagnation line translation-rotation temperature and vibration temperature, where $n = 0$ corresponds to the sphere stagnation point. In this and each following figure, n represents the direction normal to the surface. In each figure of this section, the solid lines represent the shock-fitting computation and the dashed lines represent validation data. A large discrepancy in the computed temperatures can be seen near the shock at approximately $n = 0.054$ cm. This is most likely due to the different computational methods used and the different grid stretching in the wall normal direction. The shock-fitting method used in this paper uses Rankine–Hugoniot relations to compute the temperature behind the shock, whereas shock-capturing methods capture the shock and are commonly more diffusive near the shock. Similar results from Prakash et al. [19,25] also show a discrepancy in computed temperatures behind a shock for thermochemical nonequilibrium flow between a shock-fitting method and a shock-capturing method.

The shock standoff distance on the stagnation line for the shock-fitting method is 0.0515 cm. It is difficult to tell exactly where the shock lies for the shock-capturing method. The shock is located at 0.050 cm for the shock-capturing method, assuming the shock lies at the maximum of translation-rotation temperature. This yields a 3% relative difference between the two methods, which is adequate. There is a discrepancy in the temperature equilibration location for the shock-fitting method ($n \approx 0.045$ cm) and the shock-capturing method ($n \approx 0.035$ cm). For the shock-fitting method, the distance between the shock and the equilibration point is less. For the shock-capturing method, there is a much larger difference between the translation-rotation temperature and the vibration temperature behind the shock. This makes the vibration temperature increase more quickly than the shock-capturing method, thus moving the equilibration point nearer to the shock. Physically, the shock thickness will be thin when the continuum approximation is valid, as it is here. The equilibration point of the shock-fitting method may be physically more accurate, as the shock is approximated as a line for a two-dimensional calculation and the shock-capturing method smears the shock over multiple grid points. This means that, for the shock-fitting method, the vibration temperature is exactly its freestream value after the shock because it has not had time to relax, whereas for the shock-capturing method, the vibration temperature rises across the shock due to shock smearing.

A comparison of contour lines for the entire computational domain of vibration temperature and $1 - T/T_v$ is given in Fig. 2. Only the

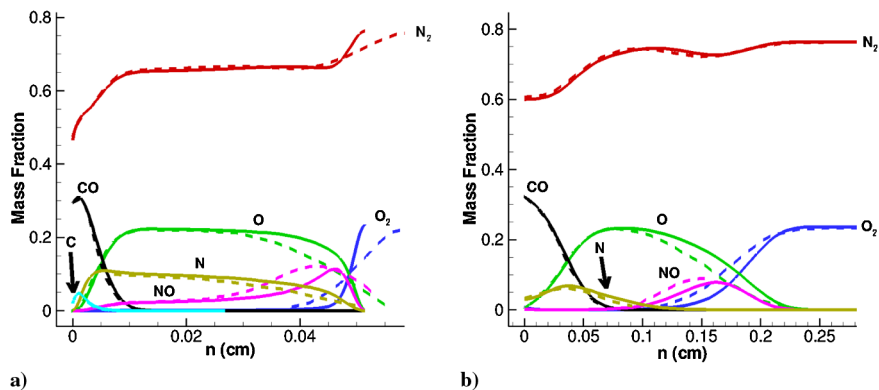


Fig. 3 Comparison of a) mass fractions on the stagnation line, and b) mass fractions at the sphere exit. Dashed lines are from [4], and solid lines are from the current simulation.

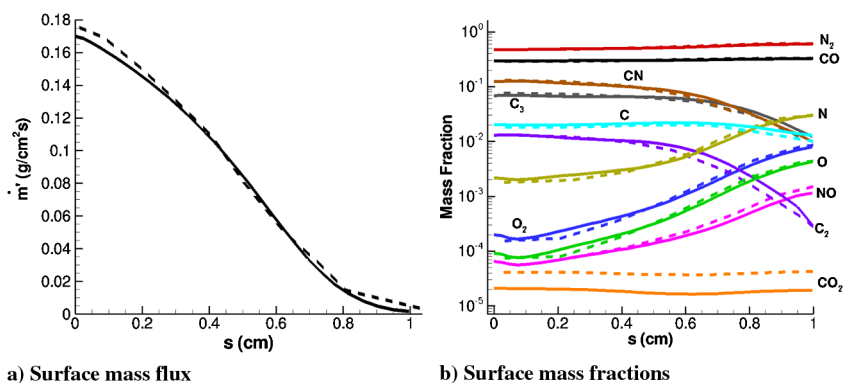


Fig. 4 Comparison of surface values to [4], where s is measured on the surface streamline and $s = 0$ corresponds to the stagnation point. Dashed lines are from [4], and solid lines are from the current simulation.

lines that were clearly distinguishable from [4] are used for comparison. The discrepancy between the two methods is the most pronounced near the shock, similar to the discrepancy in stagnation line temperatures. Near the body, there is a good agreement between the two methods. The simulated T in the computational domain will be in good agreement with [4], as T_V and $1 - T_V/T$ are in good agreement.

A comparison of the stagnation line mass fractions and the mass fractions at the sphere exit are given in Fig. 3 to ensure the gas phase reactions are implemented correctly. For both subfigures, the comparison between the mass fractions shows only small discrepancies toward the surface ($n \approx 0$) where the computed temperatures between the two methods are similar. N_2 dissociates faster near the shock for the shock-fitting method due to higher simulated temperatures resulting in a slight discrepancy. As the flow moves toward the body, the temperature discrepancy is smaller and the mass fraction of N_2 compares well. Near the shock, there are discrepancies in the mass fractions of O_2 , O , and NO due to a higher temperature computed by the shock-fitting method. This causes higher reaction rates and faster dissociation of O_2 .

A comparison of the surface chemistry model was obtained by comparing the total surface mass flux \dot{m}' and the surface mass fraction of each species, shown in Fig. 4. The surface streamline is s and is measured starting from the stagnation point. It should be noted that the data from [4] were digitized from a plot where the scale was small, leading to the jumpiness in the data of Fig. 4a, which was not in the original plot. Good agreement is obtained for the surface mass flux. There is a 3% relative difference at the stagnation point in surface mass flux, and the profiles of the two computations are similar. The location $s \approx 1$ cm corresponds to the sphere exit and, at this point, the mass flux is close to zero, so for this case, most of the ablation occurs near the nose as expected. In Fig. 4b, the surface mass fractions are compared. The comparison between each species is adequate with a large relative difference in CO_2 . The trend in CO_2 is

similar, and the absolute value of CO_2 is on the order of 10^{-5} . It is possible that small differences in temperature or more concentrated species such as O_2 may lead to the large relative difference in CO_2 due to the complex interplay between model parameters. Recall from Sec. IV that CO_2 is not produced at the surface, so it must be formed in a gas phase reaction (reactions 5, 13, 20, and 23), which is dependent upon temperature and species concentrations. It is also possible that this discrepancy may be attributed to the different truncation errors for the different methods.

B. Comparison to $M_\infty = 15.99$ Simulation of PANT Case 2

A second case was compared with [4] and is called PANT case 2, as the flow conditions come from the PANT program. Similar to PANT case 1, the geometry is a sphere and the grid has 32 points on the surface and 91 points in the surface-normal direction. A curve fit to the surface temperature profile from [4] is used for a more reasonable comparison. The freestream conditions for this case are given in Table 2.

Similar to PANT case 1, a comparison of contour lines for the entire computational domain of T_V and $1 - T_V/T$ are given in Fig. 5. Only the lines that were clearly distinguishable from [4] are used for comparison. Assuming T_V and $1 - T_V/T$ compare well, T will also compare well. For this case, the two methods agree well throughout

Table 2 Freestream conditions for PANT case 2

Parameter	Value
M_∞	15.99
ρ_∞	2.4093×10^{-1} kg/m ³
p_∞	20260.0 N/m ²
C_{N_2}	0.7635
C_{O_2}	0.2365

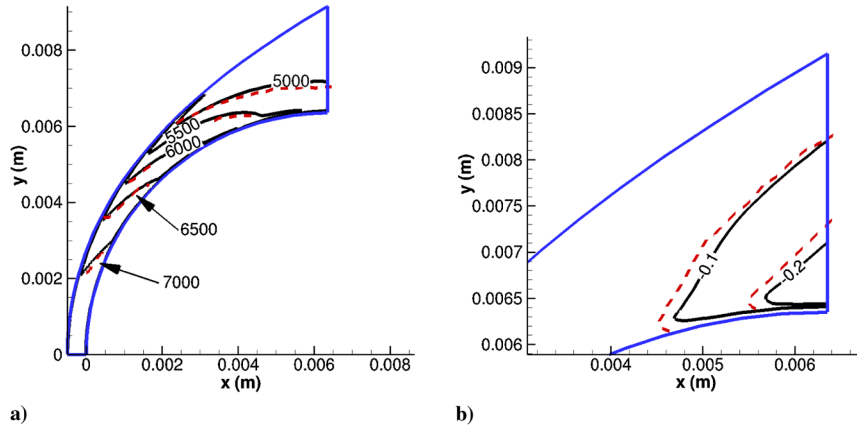


Fig. 5 Comparison of a) T_V contours, and b) $1 - T/T_V$ contours, where the dashed lines are from [4] and the black lines are from the current simulation.

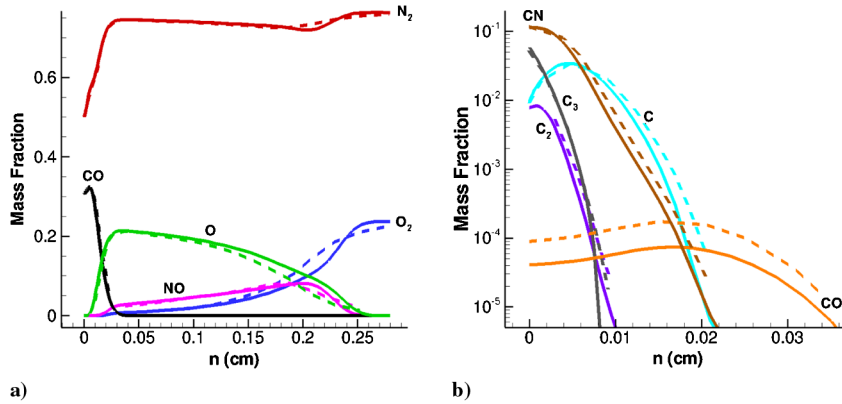


Fig. 6 Comparison of a) mass fractions at the sphere exit, and b) a close-up of the mass fractions at the sphere exit. Dashed lines are from [4], and solid lines are from the current simulation.

the entire domain. The discrepancies in temperature directly downstream of the shock are not as pronounced here as they are in PANT case 1. This is most likely due to the larger freestream density leading to a quicker equilibration of the two temperatures.

The mass fractions at the sphere exit plane are compared in Fig. 6. Similar to PANT case 1, there is a good agreement near the wall and there is some difference near the shock due to a higher computed translation-rotation temperature for the shock-fitting method. In Fig. 6b, a close-up of the mass fractions at the sphere exit is given. Similar to PANT case 1, there is adequate agreement in all the species with a large relative difference in CO_2 . The trends of CO_2 on the stagnation line are similar, but the shock-fitting value is slightly lower. Also, the value of CO_2 is quite small, being on the order of 10^{-4} , which is low enough to not affect the computational results for this case significantly. The reason for the large relative difference may be attributed to small changes in more concentrated species or differing truncation errors for the two methods, similar to the results for PANT case 1.

Figure 7 compares the surface mass flux. The surface streamline is s and is measured from the stagnation point. At the stagnation point, there is a 7% relative difference between the two computations and the maximum relative difference is 17% at $s = 0.142$ cm. In [4], it is noted that the maximum mass flux should occur at the stagnation point so the increase in mass flux after the stagnation point is not physical. Also, it is noted that the modified Steger–Warming scheme that is used in the shock-capturing method has some numerical issues near the stagnation point. Taking these points into account, the decreasing mass flux with a maximum at the stagnation point seen in the shock-fitting method is physically more accurate.

Overall, the comparison between the shock-fitting method and [4] for PANT cases 1 and 2 is good. The mass fractions of the gas species compare well throughout the domain and at the surface, suggesting that the gas phase reactions as well as the surface boundary conditions

have been implemented correctly. The two temperatures compare accurately for PANT case 2 and have some discrepancy near the shock for PANT case 1. The discrepancies seen in PANT case 1 are suggestive of the different numerical methods used and different grid types used rather than incorrect implementation.

C. Comparison to $M_\infty = 5.84$ Graphite Ablation Case

A third case was simulated to compare the gas model and surface chemistry model to simulations performed by Chen and Milos [6] of a sphere cone geometry with graphite ablation. This test case was chosen to compare with computations as well as an experiment

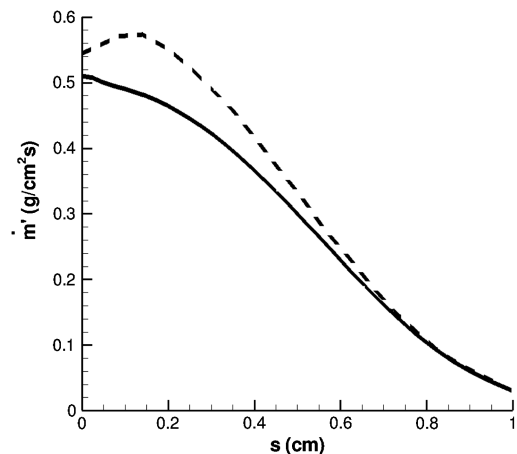


Fig. 7 Comparison of surface mass flux, where s is measured on the surface streamline and $s = 0$ corresponds to the stagnation point. The dashed line is from [4], and the solid line is from the current simulation.

Table 3 Freestream conditions for Chen and Milos's case [6]

Parameter	Value
M_∞	5.84
ρ_∞	3×10^{-3} kg/m ³
p_∞	1671.36 N/m ²
C_{N_2}	0.6169
C_{NO}	0.0046
C_N	0.1212
C_O	0.2573

performed at the Interactive Heating Facility at NASA Ames Research Center. A surface temperature was measured during this experiment, so instead of computing the surface temperature from a surface energy balance, a curve fit to the experimental data is used. In [6], a different gas chemistry model than the model in the shock-fitting method is used and several surface chemistry models were tested. None of the surface chemistry models tested in [6] matched the model presented here. The nose radius was $r = 1.905$ cm, and the cone half-angle was 10 deg. The grid had 42 points on the surface and 101 points in the surface-normal direction. The freestream conditions are given in Table 3.

Figure 8 shows the comparison of the sphere surface mass blowing rates and the sphere surface pressure. The dashed lines represent digitized data from [6], the symbols represent the experiment, and the solid line represents current computations. Four different types of surface chemistry models are used in [6] for one set of freestream conditions. Park (nitridation) represents a surface chemistry model from [11,43,44] containing oxidation, nitridation, and sublimation of C_3 . Park (no nitridation) represents the same model with the surface nitridation reaction turned off. A chemical equilibrium boundary condition represents that the gas phase and ablation boundary conditions are in equilibrium, and the remaining surface chemistry model is a finite-rate model proposed by Zhluktov and Abe [10], which includes oxidation, sublimation, and recombination, but no nitridation.

The ablation boundary conditions used in the shock-fitting code represent the two experimental data points the best. In Fig. 8a near the stagnation point, the current computations are almost identical to the experiment. This was not obtained by changing model parameters, but rather, the model just happens to represent this particular dataset quite accurately. The shock-fitting surface chemistry model is closest to the assumption of chemical equilibrium at the surface. The mass flux is less than the Park model with nitridation [11,43,44]. The current surface chemistry model does not include nitridation but does include recombination of atomic oxygen and sublimation of C and C_2 , which is not included in the Park model with nitridation. Since sublimation of C and C_2 is small, the difference between the two models is mainly due to the added nitridation reaction as well as slight

variations in the reaction probabilities. When the nitridation reaction is turned off, the current surface chemistry model has a greater mass flux than the Park model. A comparison to the complex model of Zhluktov and Abe is not as straightforward [10]. Zhluktov and Abe accounted for many more reactions and accounted for active sites where chemical processes can take place. Near the stagnation point at the first available data point, there is a 33% relative difference between Zhluktov and Abe and the current computations. The absolute difference between the models decreases along the surface streamline, but the relative difference increases to 81% at $s = 2.66$ cm.

Figure 8b shows the sphere surface pressure profiles from the shock-fitting method and [6] using the Park model with nitridation. The exact surface pressure boundary condition used in [6] was not available, whereas the pressure condition used in the shock-fitting code for this case is the one-dimensional characteristic boundary condition for a subsonic inlet. The pressure obtained by the two methods shows a good agreement considering that the gas phase chemistry models are different as well as the surface chemistry model.

A comparison of the species mass fraction along the stagnation line is given in Fig. 9. The solid lines represent the shock-fitting code, and the symbols represent [6] with the Park nitridation surface chemistry model [11,43,44]. There is a good comparison for the standard air species. Near the wall, the mass fraction of O_2 increases significantly for the shock-fitting method, whereas it decreases for [6]. This is because the Park nitridation model [11,43,44] does not include surface recombination of atomic oxygen, whereas it is included in the shock-fitting surface chemistry model. The mass fraction for CN is higher at the wall for the Park nitridation model because nitridation is included, whereas it is not in the shock-fitting model. There exists

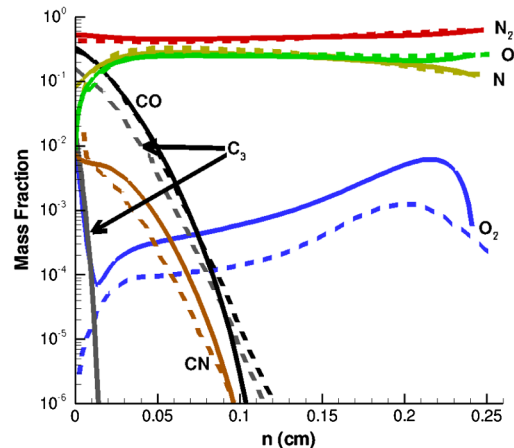


Fig. 9 Comparison of species mass fraction along the stagnation line to [6]. Dashed lines are from [6], and solid lines are from the current simulation.

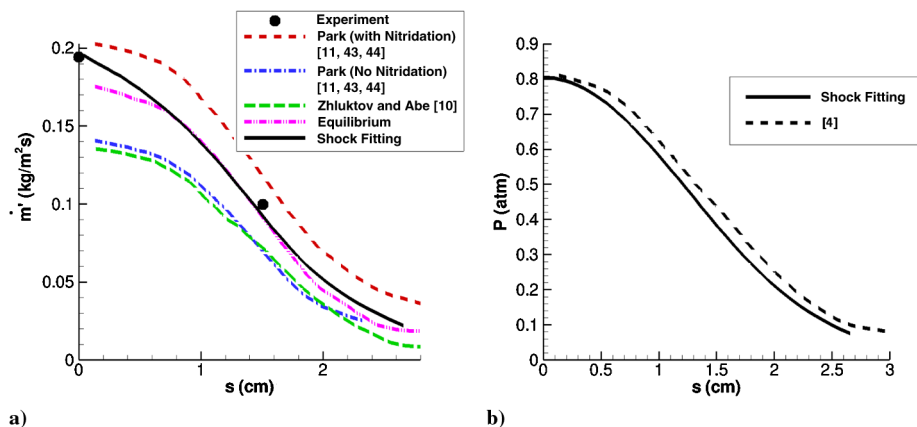


Fig. 8 Comparison of a) sphere surface mass blowing rates, and b) sphere surface pressure. Dashed lines are from [6], and solid lines are from current simulation.

a significant difference in the mass fraction of C_3 . In the shock-fitting code, the mass fraction of C_3 decreases quickly along the stagnation streamline and reaches 10^{-5} at approximately 0.1 mm from the surface. For [6], C_3 decreases but not as quickly, and it reaches 10^{-5} at approximately 1 mm from the surface. While part of this may be attributable to diffusion ([6] uses $Le = 1$, whereas shock-fitting uses $Sc = 0.5$), most would be attributed to differences in the gas model. Chen and Milos [6] only included dissociation of C_3 , whereas the shock-fitting gas model includes dissociation of C_3 and two exchange reactions (reactions 17 and 21) involving C_3 . These exchange reactions give two more pathways for C_3 to react and change chemical composition, most likely leading to the difference between the two simulations.

For this case, it was seen that the gas and surface models implemented in the shock-fitting method compare well with other gas and surface models implemented in validated research codes. This suggests that the models are consistent with other validated models. The surface mass flux for the shock-fitting method compares well with the limited experimental data, suggesting that the current model is adequately simulating graphite ablation for the experimentally tested conditions.

VI. Direct Numerical Simulation of $M_\infty = 15.99$ Blunt Cone

After validating the new shock-fitting method, direct numerical simulations are performed using the new high-order shock-fitting thermochemical nonequilibrium method, with graphite ablation boundary conditions to study hypersonic boundary-layer receptivity and instability with real-gas effects and graphite ablation effects over a blunt cone. A DNS is composed of two distinct simulation results: 1) the simulation of the steady laminar base flow, and 2) the simulation of freestream disturbances imposed on the steady base flow. The steady base flow is laminar, with no turbulence model, and must be extremely numerically convergent or small amplitude waves will be overcome by numerical noise. Once the base flow is converged within predefined tolerances, linear (i.e., small amplitude) noninteracting freestream fast-acoustic waves are imposed on the steady laminar base flow in the freestream. As the freestream waves cross the shock and enter the boundary layer, the receptivity process has begun. Receptivity links the linear freestream waves with the initial conditions of disturbance amplitude, frequency, phase, etc., for the breakdown of laminar flow. Boundary-layer receptivity to freestream disturbances has been reviewed by Saric et al. [45] and, more recently, covered by Fedorov [46] as part of the hypersonic boundary-layer transition process. After receptivity in a low disturbance environment, modal growth occurs where the second mode is commonly the dominant mode for flat plates and sharp cones at a zero angle of attack. The second mode originates after the synchronization location from either mode S or mode F , which are termed for their similar phase speeds to slow and fast-acoustic waves, respectively, as they separate from the continuous spectrum. Eigenmode growth provides initial conditions to nonlinear breakdown, making it essential to understand eigenmode growth as well as receptivity to accurately predict transition.

The receptivity and eigenmode growth process in a low freestream disturbance environment for flat plates and cones has been studied extensively for perfect-gas flows, but there is a limited amount of information and some uncertainty as to how a real gas affects these processes. Zhong and Wang [47] review the current progress of DNS on hypersonic boundary-layer receptivity, instability, and transition. They point out the small amount of DNS research into real-gas flows and the need for progress in this area. The purpose of this simulation is to look at real-gas effects and ablative effects on the second mode by comparing a real-gas simulation with two perfect-gas simulations.

A. Real-Gas Steady-State Solution of $M_\infty = 15.99$ Blunt Cone

The geometry is a sphere cone with a nose radius of 0.00635 m and a cone half-angle of 7 deg. The freestream conditions are the same as the first validation case, named PANT case 1, and are listed in Table 1. The cone axis is aligned with the freestream flow, yielding an angle of attack

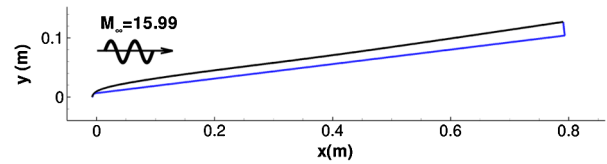


Fig. 10 Simulation domain for 7 deg half-angle blunt cone. The shock is black, and the wall and outlet are lighter colored.

equal to zero. The laminar flow over a cone at zero angle of attack is axisymmetric. Thus, only a two-dimensional axisymmetric flowfield is simulated where the transverse direction is treated by Fourier collocation. The freestream unit Reynolds number and stagnation enthalpy are $Re_u = 7.3 \times 10^6/m$ and $h_{o,\infty} = 15.3$ MJ/kg, respectively. This is a high-enthalpy case where thermochemical nonequilibrium effects are significant and still present well downstream of the nose. Figure 10 shows the simulation domain, where the shock is shown by the darker line and the wall and the outlet are shown by the lighter line.

A grid convergence study was performed to ensure that the computational grid was sufficient to capture the mean flow as well as the unsteady flowfield disturbances. The grid density in the streamwise direction was chosen to adequately resolve the highest imposed perturbation frequency (525 kHz). There are 3155 grid points in the streamwise direction. The grid in the wall-normal direction was tested with 240, 480, and 720 points. The mean flow solution was computed for each case, and then unsteady simulations were run. Figure 11 shows the surface pressure perturbation for the highest imposed frequency using the three different grid densities. The maximum relative error between the 480 and 720 simulations is 2.3% at $s = 0.75$ m. Other variables at different locations were checked as well and showed similar relative errors. For lower frequencies, the relative error is less than the highest imposed frequency. The 480 wall-normal grid point solution is grid converged.

A steady-state contour plot of the translation-rotation temperature and the vibration temperature for the thermochemical nonequilibrium case is given in Fig. 12. It is difficult to clearly visualize the entire computational domain because of its shape, so only the nose region and start of the cone frustum are displayed for the sake of clarity. The translation-rotation temperature reaches its maximum value of 14,783 K directly behind the normal shock at the stagnation line, but then it cools as the flow moves downstream. The vibration temperature reaches its maximum value of 8198 K at approximately $x = -0.68$ cm along the stagnation line. The shock angle decreases as the flow moves downstream, resulting in lower temperatures directly downstream of the shock. On the cone frustum, the vibration temperature is higher than the translation-rotation temperature near the boundary-layer edge, indicating thermal nonequilibrium. In this region, the vibration temperature is relaxing toward the lower translation-rotation temperature.

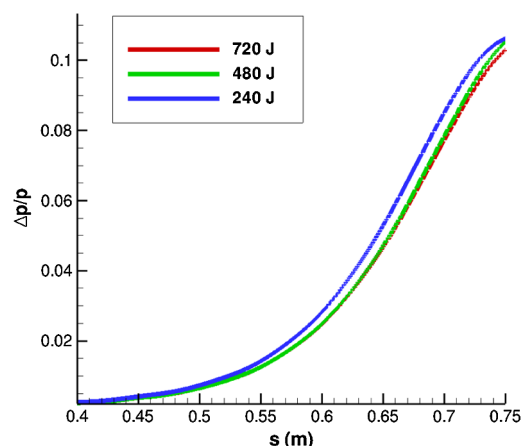


Fig. 11 Grid convergence study with three different grid densities in the wall-normal direction for the 525 kHz surface pressure perturbation.

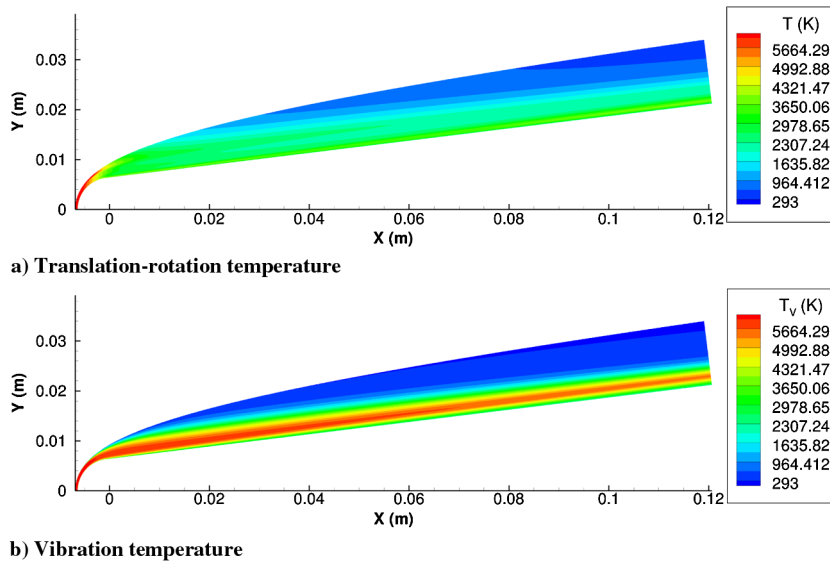


Fig. 12 Contour plots of T and T_v .

Unlike many simulations of hypersonic boundary-layer receptivity, neither is the wall temperature constant nor the adiabatic condition ($\frac{\partial T}{\partial n} = 0$) enforced. Instead, for a flow where ablative effects are considered, a surface energy balance [Eq. (54)] may be solved that yields a varying temperature profile. The temperature profile for this flow is shown in Fig. 13a. Recall that the surface is assumed to be in thermal equilibrium, meaning $T_v = T$ at the surface. The temperature has a maximum at the stagnation point and then drops rapidly as the flow expands. Surface temperature in hypersonic flows with ablation is important, as the wall temperature directly determines the reaction rate and probability for oxidation. It also plays a role in sublimation. In this case, as the wall temperature drops, the wall mass flux should drop as well. Note that the temperature of the wall is decreasing, which corresponds to wall cooling, which is stabilizing to first mode waves and destabilizing to second-mode waves. Also note that, for $0.2 \text{ m} \leq s \leq 0.8 \text{ m}$, $0.14 \geq T_w/T_0 \geq 0.13$, where T_0 is the stagnation temperature.

As temperature determines, to a large degree, surface mass loss due to ablation, the surface blowing profile should be similar to the surface temperature profile. To help visualize the blowing profile caused by chemical reactions at the surface, Fig. 13b shows the wall mass flux per area nondimensionalized by the freestream mass flux per area. This nondimensionalization is chosen because it is common in stability literature with wall blowing. As expected, the largest mass flux is at the stagnation point (approximately 1% of the freestream mass flux), corresponding to a maximum in wall temperature where the oxidation reactions as well as the sublimation reactions are all

significant. Notice the surface mass flux drops nearly two orders of magnitude across the cone nose and remains roughly the same order of magnitude along the cone frustum, indicating that outgassing effects would likely be most significant upstream in the nose region. This rapid drop of wall mass flux also corresponds to a rapid decrease in sublimation, which is shown in Fig. 14. The fact that there is still wall blowing in the cone frustum is due to the oxidation reactions. The wiggle near the nose of the cone is located directly downstream of the beginning of the cone frustum. The discontinuity in the surface curvature is likely the cause for the wiggle, and the appearance of the wiggle is exaggerated by use of a logarithmic scale.

The surface mass flux is created by interaction of the graphite ablator and the surrounding flow. To help understand the chemical processes at the surface, Fig. 14 shows the mass fraction for each species at the surface. The species with the largest mass fraction at the surface is N_2 , but it does not react with the surface. The next largest mass fraction is CO . Recall from Eqs. (39) and (40) that the carbon surface can react with O and O_2 to form CO . These two reactions are the dominate reactions for the entire length of the surface, i.e., they are responsible for the most mass loss due to ablation at the surface. Sublimation of C_3 [Eq. (49)] is an order of magnitude less than CO at the stagnation point. In the sphere region, it is the dominate sublimation product. There is a significant mass fraction of CN at the surface, even though a nitridation reaction is not taken into account in the surface chemistry model. CN at the surface is due to reactions of ablation products with N_2 and NO . For the entire length of the cone frustum, CO contains the most mass of the carbon-containing

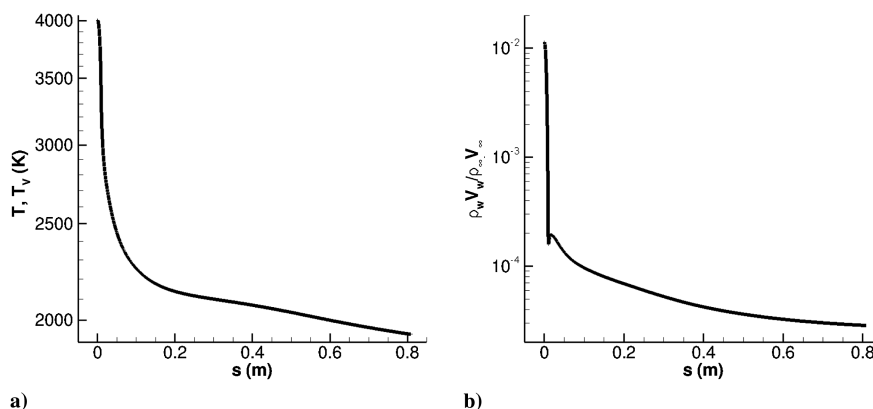


Fig. 13 Surface a) temperature, and b) nondimensional mass flux. Surface is in thermal equilibrium.

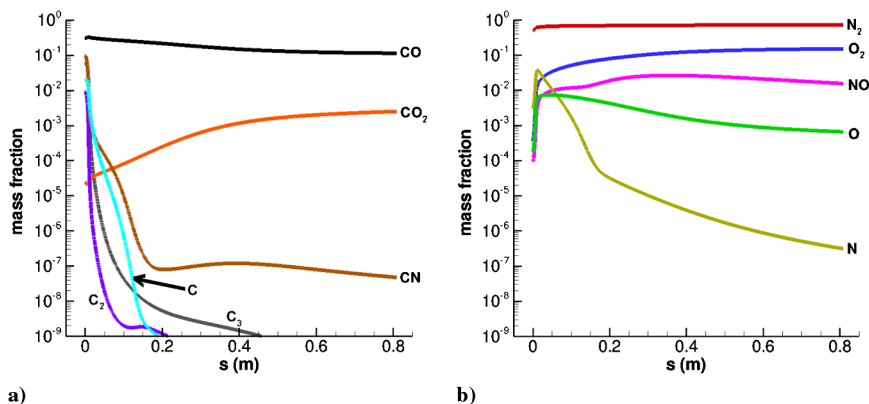


Fig. 14 Surface mass fraction for a) carbon-containing species, and b) air species.

species. This shows that CO is the species most likely to have the largest effect on boundary-layer receptivity and instability over the blunt cone.

To visualize the species mass concentrations in the surface-normal direction, a surface-normal plot is given in Fig. 15, which shows species mass fractions at $s = 0.6$ m. Only flowfield species with a mass fraction above 10^{-4} are shown. The velocity and thermal boundary layers in this figure are at $y_n \approx 4$ mm. Outside of the boundary layer, the flowfield is mainly composed of N_2 and O_2 . Inside the boundary layer, the temperature increases and chemical reactions become significant. Notice that, similar to Fig. 14a, CO and CO_2 have the largest mass concentration of the carbon-containing species. Neither of these species diffuses to the boundary-layer edge with a mass concentration greater than 10^{-4} . The critical layer for a hypersonic boundary layer approaches the boundary-layer edge for high-Mach-number flows such as the $M_\infty = 15.99$ flow simulated here. Large disturbance amplitudes for species densities are expected at the critical layer for second-mode instabilities. Since no carbon-containing species diffuse significantly to the boundary-layer edge, it is likely that the effects of the carbon-containing species are minimal, as they are mainly constrained to the near-surface region and not significantly present near the critical layer.

B. Comparison with Ideal-Gas Steady-State Solutions

To investigate real-gas and blowing effects, three separate steady solutions were computed for receptivity and instability simulations. The first is the full thermochemical nonequilibrium shock-fitting method with graphite ablation, described in Sec. VI.A. The other two cases are ideal-gas cases, which use the same nonequilibrium code with the source terms turned off, the vibration energy held constant, and the mass fractions held to their freestream value. This is done so

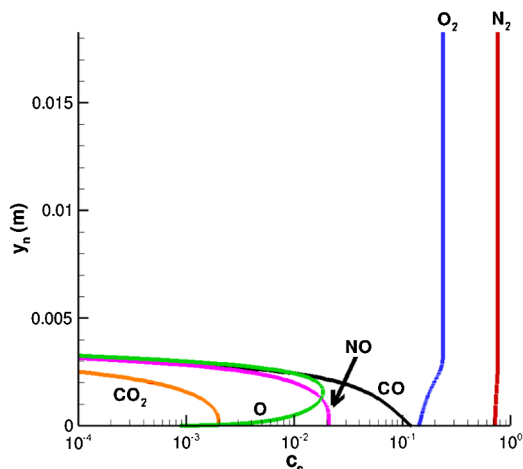


Fig. 15 Species mass fraction in surface normal direction for $s = 0.6$ m.

the viscosity, thermal conductivity, etc., are calculated the exact same way for the nonequilibrium and ideal-gas cases, therefore making differences in the simulations due to the gas types and not the models used for each type. The first ideal-gas case uses the temperature at the wall boundary from the thermochemical nonequilibrium graphite ablation case with the no-slip boundary condition. The second ideal-gas case matches the wall temperature as well as the wall mass flux of the thermochemical nonequilibrium graphite ablation case. This is done to test the effects of thermochemical nonequilibrium and wall mass flux on boundary-layer stability. For ease of discussion, the two ideal-gas cases will be called "ideal gas" and "ideal-gas blowing," whereas the full thermochemical nonequilibrium ablation case will be called "real gas."

A comparison of each of the current cases' shock-layer profiles are given at two separate streamwise locations in Fig. 16, where u_t represents the velocity tangent to the surface, and y_n is the wall-normal coordinate. These two profiles are located on the cone frustum, and the shock height is demarcated at the top of each profile. Both ideal-gas cases have a larger shock height than the real-gas case, and the difference becomes less moving downstream, as expected. The two ideal-gas cases have similar boundary-layer profiles, and the real-gas profile is approaching the ideal-gas profile downstream as real-gas effects become less significant. Similarly for temperature, the ideal-gas cases are similar and the translation-rotation temperature is nearing the ideal-gas solution downstream. Notice that the height of both the thermal and velocity boundary layers is similar, i.e., there is not a large difference between the boundary-layer thicknesses. It has been shown in previous experimental research that the height of the boundary layer is nearly half the wavelength of the dominant second-mode instability [48]. The phase velocity of the dominant instability mode can be roughly approximated as the boundary-layer edge velocity, which is nearly constant away from the blunt nose. Since $c_r \approx \text{const.} \approx 2\pi f / \alpha_r \approx 4\pi\delta f$ where δ is the boundary-layer thickness, it is expected that the frequency range for unstable disturbances would be similar for all three cases. If the frequency range of unstable second-mode disturbances is similar, then differences in second-mode growth would be due more to differences in growth rate rather than different unstable frequency ranges.

C. Hypersonic Boundary-Layer Receptivity and Instability Results

After simulating the steady base flow, an unsteady simulation was performed. It was assumed a priori that the dominant instability mode for the freestream conditions and geometry would be the second mode. The second mode is most unstable when its phase velocity is aligned with the freestream flow. Therefore, an unsteady two-dimensional axisymmetric simulation was performed to minimize the required computing resources.

Freestream disturbances were imposed on the steady base flow to find how the boundary layer behaved in the presence of graphite ablation and thermochemical nonequilibrium. The freestream disturbances imposed were weak planar fast-acoustic waves in the freestream before reaching the shock at a zero incidence angle.

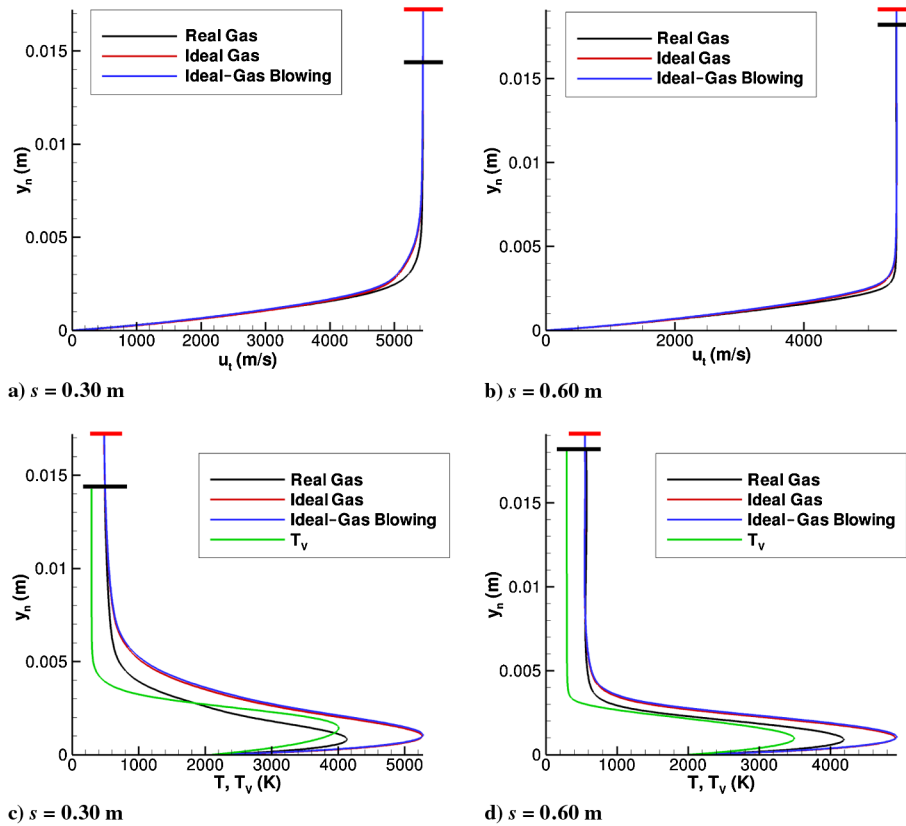


Fig. 16 Steady-state profile comparison between the three simulation cases for two streamwise locations. Shock heights are marked for clarity.

The freestream variables can be written as a summation of the mean flow and an oscillating perturbation as

$$\begin{bmatrix} \rho_{1,\infty} \\ \vdots \\ \rho_{ns,\infty} \\ u_{1,\infty} \\ p_\infty \end{bmatrix} = \begin{bmatrix} \bar{\rho}_{1,\infty} \\ \vdots \\ \bar{\rho}_{ns,\infty} \\ \bar{u}_{1,\infty} \\ \bar{p} \end{bmatrix} + \begin{bmatrix} \Delta\rho_{1,\infty} \\ \vdots \\ \Delta\rho_{ns,\infty} \\ \Delta u_{1,\infty} \\ \Delta p_\infty \end{bmatrix} \exp(i(k_{x,\infty}(x - (u_{1,\infty} + c_\infty))t)) \quad (59)$$

where the disturbance amplitudes for fast-acoustic waves are defined by

$$\epsilon = \frac{\Delta p_\infty}{\gamma_\infty p_\infty} = \frac{\Delta \rho_\infty}{\rho_\infty} = \frac{\Delta u_{1,\infty}}{c_\infty} \quad (60)$$

Here, γ_∞ is the ratio of specific heats in the freestream, c_∞ is the speed of sound in the freestream, and $\epsilon = 5 \times 10^{-4}$. Seven frequencies are imposed, starting with a base frequency of 75 kHz, where each frequency is a multiple of this base and the last frequency is 525 kHz. All frequencies are imposed simultaneously, and their phases are set randomly.

For each of the three unsteady cases, the simulation was run until the solution became periodic in time. After which, the simulation was run for one more full period in time and data were output for a temporal Fourier analysis. The Fourier analysis decomposed the flowfield disturbances back to the original seven imposed freestream frequencies, giving the amplitudes and phase angles of all saved variables for each frequency in the following form:

$$\phi'(x, y, t) = \Delta\phi(x, y) \exp[i(\psi(x, y) - 2\pi ft)] \quad (61)$$

where ϕ' is the perturbation of some variable, $\Delta\phi$ is the amplitude of that variable, ψ is the corresponding phase angle, and f represents a single dimensional frequency. An instantaneous snapshot of the flowfield can be obtained from the real part of ϕ' when t is specified.

In a DNS, many boundary-layer modes are present in the boundary layer simultaneously. As one mode becomes dominant for a given frequency, it is possible to derive equations for the growth rate, wave number, and phase speed of this mode from Eq. (61), which yields

$$-\alpha_i = \frac{1}{\Delta\phi(f)} \frac{d}{ds} \Delta\phi(f) \quad (62)$$

$$\alpha_r = \frac{d}{ds} \psi(f) \quad (63)$$

$$c_r = \frac{2\pi f}{\alpha_r} \quad (64)$$

where s is the streamwise coordinate, $\Delta\phi(f)$ represents a variable amplitude at a given frequency, $\psi(f)$ represents the corresponding phase angle at the given frequency, and $\alpha_i < 0$ indicates instability. It is possible to compute α_i , α_r , and c_r using variables that peak at the critical layer for second-mode disturbances. If this is done, interpolation may be required to trace the critical layer downstream. In this work, surface pressure is used as a second-mode pressure disturbance, has a maximum amplitude at the surface, and no interpolation is required. Previous researchers [49] have used surface pressure perturbations to compute α_i , α_r , and c_r from a DNS, which compared well with theoretical results.

An accurate comparison of growth rate, wave number, and phase velocity of an individual instability mode may be obtained between DNS and linear stability theory (LST) results when the particular boundary-layer instability mode is dominant, i.e., its magnitude is larger than magnitudes of other instability modes simultaneously present in the boundary layer. This is the case in many hypersonic boundary layers where the second mode grows exponentially and dominates other instability modes. If a dominant instability mode is not present, then wave modulation occurs due to multiple instability modes of similar magnitudes. In this work, an 11-species real-gas

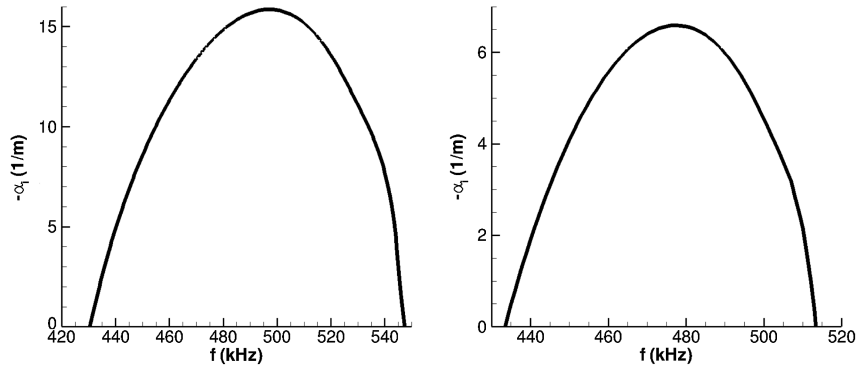


Fig. 17 Unstable frequency range at $s = 0.60$ m obtained from LST.

LST code with ablative boundary conditions that accounts for transverse curvature developed by Mortensen and Zhong [50] is used for comparison to DNS results and to compute some boundary-layer characteristics such as unstable frequency ranges. Also, ideal-gas LST results are used, which are obtained from a derivative of the real-gas code, i.e., source terms are turned off and the vibration energy equation is neglected. LST assumes flow perturbations are in the form of a normal mode described by

$$\phi'(x, y, z) = \hat{\phi}(y) \exp[i(\alpha x + \beta z - 2\pi f t)] \quad (65)$$

where x is aligned with the surface, y is the surface normal direction, z is the transverse direction, $\hat{\phi}$ is the complex eigenfunction, and α and β are the wave numbers. The spatial stability approach is used, where α is complex, α_r is the wave number, and $\alpha_i < 0$ represents modal growth. Second-mode growth is a maximum for $\beta = 0$, which represents a two-dimensional axisymmetric instability.

Before moving further, the unsteady DNS boundary conditions for each simulation need to be addressed. For each of the three cases, different unsteady wall boundary conditions are imposed. Each case uses pressure extrapolation to set the disturbance wall pressure. For the real-gas case, the surface mass balance as well as the surface energy balance are used as boundary conditions. This means that the wall-normal velocity will fluctuate as well as the wall temperature. For the ideal-gas case, the no-slip condition is enforced on the disturbances and $T'_w = 0$. For the ideal-gas blowing case, the mass flux is forced to remain constant and $T'_w = 0$. When enforcing the mass flux to remain constant, the wall-normal velocity must fluctuate because density will fluctuate at the surface [recall Eq. (57)].

An unstable frequency range for the second mode at $s = 0.60$ m was computed using LST and is shown in Fig. 17. A positive growth rate $-\alpha_i$ indicates an unstable second mode, whereas a negative growth rate indicates a stable second mode. LST predicts for the real-gas case at this streamwise location that the second mode will be unstable between 430 and 547 kHz. The growth rates for the 450 and 525 kHz second modes are 12.4 and 8.6, respectively. The DNS shows that the 525 kHz second mode would be unstable and the

450 kHz second mode would be unstable as well, indicating an agreement between the two methods. A similar agreement was obtained upstream near $s = 0.30$ m for the real-gas case where the 525 kHz disturbance is unstable in the DNS and is predicted to be unstable by LST. Figure 17b shows the unstable frequency range predicted by LST for the ideal-gas blowing case. The unstable range is similar for both ideal-gas cases, so only one case is shown. LST predicts that, at this streamwise location, the second mode will be unstable between 434 and 513 kHz. Therefore, it is expected that, at $s = 0.60$ m, the imposed 525 kHz disturbance will be stable in both ideal-gas simulations and the 450 kHz disturbance will show some disturbance growth. Note that the LST results were not available at the time the DNS freestream forcing frequencies were chosen, so the forcing frequencies are not tailored to the LST predictions.

For a second-mode wave, it is well known that the maximum pressure perturbation occurs at the surface and the growth of the second mode is exponential. Figure 18 shows a plot of the real part of the 525 kHz pressure perturbation at the wall for the real-gas case and the ideal-gas blowing case. The real part of the pressure perturbation mimics the instantaneous flow. The ideal-gas case is not shown, but its behavior is similar to the ideal-gas blowing case. For the real-gas pressure perturbation, exponential growth is clearly visible, indicating a dominant second mode. There is no exponential growth in the ideal-gas blowing case; there is just modulation around a relatively constant amplitude. This modulation, or pumping, indicates that no dominant mode is present, but rather multiple competing modes are present. It is possible to separate multiple competing modes through multimode decomposition, as in [51]. This is beyond the scope of the present work, as the focus here is on second-mode instability.

If there is a dominant boundary-layer mode in the DNS, it is possible to compare the growth rate, wave number, and phase speed to LST predictions of the dominant mode. A comparison of the growth rate for the 525 kHz disturbance is given in Fig. 19. The ideal-gas case is not shown, but its behavior is similar to the ideal-gas blowing case. The oscillations in the DNS growth rates comes from multiple competing modes that are all present in the boundary layer

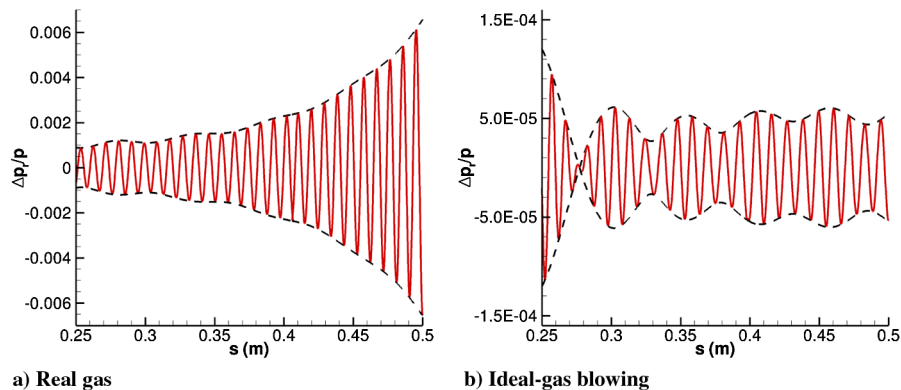


Fig. 18 Instantaneous surface pressure for 525 kHz disturbance.

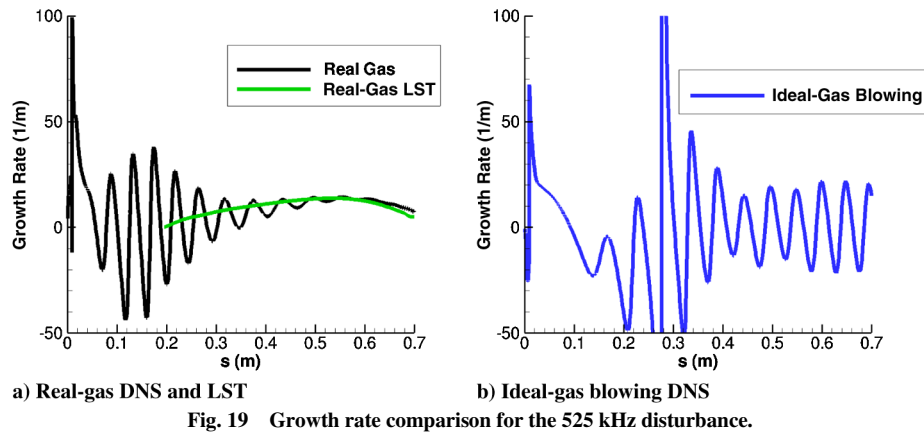


Fig. 19 Growth rate comparison for the 525 kHz disturbance.

simultaneously during the simulation where the LST growth rate is smooth because it is predicting only the second mode. For all three cases, growth can be seen near $s = 0$, which represents the stagnation location. This growth is most likely due to resonant interactions of the freestream fast-acoustic forcing waves with mode F . The real-gas DNS simulation shows second-mode growth starting near $s = 0.2$ m. The second-mode amplitude grows exponentially, starting from $s = 0.2$ m, whereas other boundary-layer modes may be stable or decay exponentially. As the second mode grows exponentially, it becomes the dominant mode. This behavior can be seen as the oscillations in the DNS growth rate gradually dampen downstream of $s = 0.2$ m. Recall from Eq. (62) that the growth rate is computed from the DNS surface pressure perturbation amplitude. As the second-mode amplitude becomes much larger than other modes in the boundary layer, the simulated growth rate from the DNS should be similar to LST predictions for the second mode. Similar growth rates between DNS and LST indicate that the modal growth from the DNS is indeed the second mode and that the second mode has become the dominant instability mode. For this complex DNS flowfield, the current comparison to LST is quite good. The two methods begin to diverge downstream ($s > 0.7$ m), where the DNS disturbance amplitudes are large enough, where nonlinear behavior cannot be neglected. As LST assumes that disturbances are linear, some difference is to be expected. It should be noted that, with significant wall cooling and surface blowing, third and higher modes could possibly become unstable. For the simulated domain, no higher modes were found for the 525 kHz frequency, although it is possible they may appear further downstream. Decreasing oscillations are not seen in the ideal-gas blowing case because there is no dominant instability mode. For the ideal-gas blowing case, it is difficult to say if there is any growth because the growth rate is so strongly oscillatory.

The wave number and phase speed for the 525 kHz disturbance is shown for all three cases in Fig. 20. An LST comparison is given for

the real-gas case, and the phase speed is nondimensionalized by the freestream velocity. An LST comparison to the two ideal-gas cases is not given, as there is no well-defined boundary-layer instability mode and the focus of this research is on real-gas effects. Once again, oscillations are seen in the DNS simulation that die out for the real-gas case as the flow moves downstream ($0.2 \geq s \geq 0.7$ m), indicating a dominating boundary-layer mode. For both the wave number and the phase speed, the LST and DNS results compare well, which increases the reliability of the results for both methods. Mode F and mode S are expected to be present simultaneously in the DNS. The phase speeds for mode F and mode S as they separate from the continuous spectrum are $c_r/u_e = 1 \pm 1/M_e$, respectively, where the subscript e represents boundary-layer edge conditions. M_e can be approximated as M_∞ for a flat plate with a weak shock. For a blunt body, such as the blunt cone simulated here, the edge conditions are not well defined due to a varying shock shape. Therefore, the flat-plate conditions for the phase speeds of mode F and mode S (i.e., $c_r/u_e \approx 1 \pm 1/M_\infty$) may be used as a guide rather than a precise measurement. Tracing the phase velocity downstream from $s = 0$ to $s \approx 0.2$ m for the two ideal-gas cases shows the phase velocity drop from 1.3 to below 0.9 as it likely approaches a synchronization point with mode S . After this synchronization point, the phase velocity then increases back to the fast-acoustic phase velocity. For the real-gas simulation, the phase velocity drops slightly below 0.9 and remains there for the length of the domain. Further work is underway to find out precisely what physical mechanisms are at play here.

It is interesting to note that the boundary-layer wave for the real-gas case has a nondimensional phase speed near unity at the domain entrance, which is indicative of an entropy/vorticity wave where, for the ideal-gas cases, the phase speed is around 1.1, indicating a fast-acoustic wave. Recall that freestream fast-acoustic waves were used in the freestream to perturb the steady base flow. Logically, it would seem that with fast-acoustic freestream forcing the incoming wave

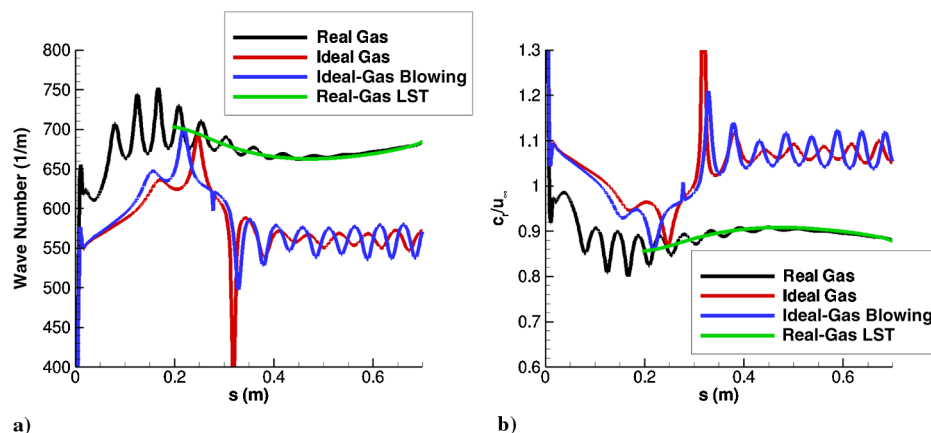


Fig. 20 Comparison of a) wave number, and b) phase velocity nondimensionalized by the freestream velocity for the 525 kHz disturbance.

would be predominantly fast acoustic as well, but it is possible that real-gas effects or surface chemistry effects are exciting the entropy/vorticity wave stronger than the ideal-gas cases.

An instantaneous snapshot of the translation-rotation temperature and vibration temperature in the real-gas perturbed flowfield for the 525 kHz frequency disturbance is shown in Fig. 21. The instantaneous snapshot is obtained by setting $t = 0$ in Eq. (61) and taking the real part of the perturbed quantity. The 525 kHz frequency is shown because it is the most unstable frequency in the real-gas simulation and second-mode behavior can clearly be seen. The top of the domain is the shock, and the bottom of the domain is the cone surface. Note that the scales for the subfigures are not the same due to exponential disturbance growth, so colors cannot be compared exactly between subfigures.

For the translation-rotation temperature contour plots, the second-mode wave can be seen in the oscillating colors near the wall and at the boundary-layer edge. This is due to a large perturbation near the boundary-layer edge and a large perturbation near the wall. The magnitude of the second-mode wave in Fig. 21a decreases slightly, indicating that the boundary-layer flow is stabilizing for this frequency component. For Figs. 21b and 21c, the second-mode wave

increases in magnitude in the downstream direction as it becomes dominant. The increase in magnitude should be exponential as second-mode growth is exponential. Exponential growth is visible by comparing Figs. 21b and 21c. Darker colors in Fig. 21b are on the order of 10^{-4} , whereas darker colors in Fig. 21c are on the order of 10^{-3} , indicating exponential growth of the second-mode wave. Above the second-mode wave are waves due to freestream forcing waves as they cross the shock in the nose region and then propagate downstream. These waves propagate downstream and toward the boundary layer with a relatively constant amplitude. Eventually, they move into the boundary layer and are dominated by the second mode. Just below the shock, waves can be seen that are a direct result of fast-acoustic freestream forcing waves propagating through the shock. There are also Mach waves that can be seen just outside of the boundary layer as the flow adjusts to disturbances.

Similar to the translation-rotation temperature, the second-mode wave can be seen in the vibration temperature contour plot with an increasing magnitude in the streamwise direction. The peak near the boundary-layer edge is much larger than the peak near the wall for vibration temperature. The perturbation just outside of the boundary layer is due to freestream forcing waves entering near the cone nose

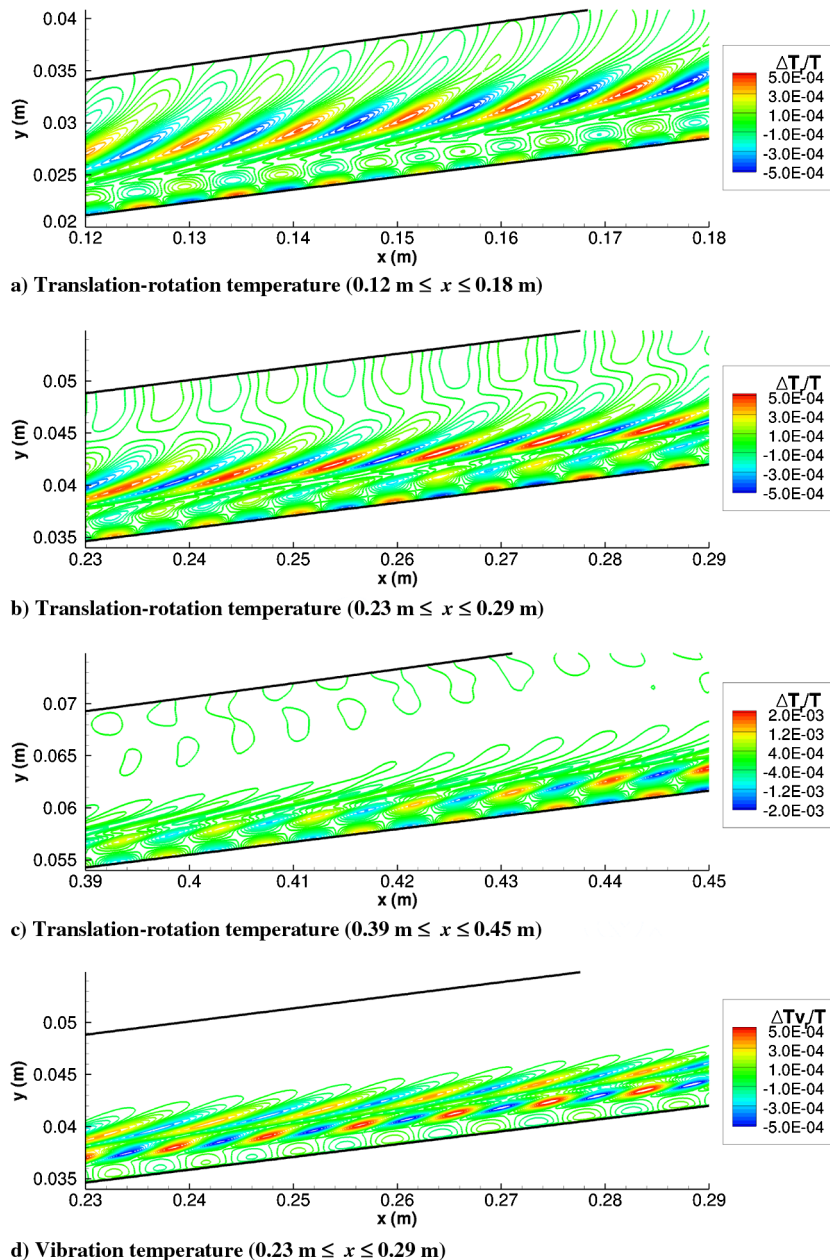


Fig. 21 Instantaneous perturbation contour plots for the 525 kHz frequency disturbance.

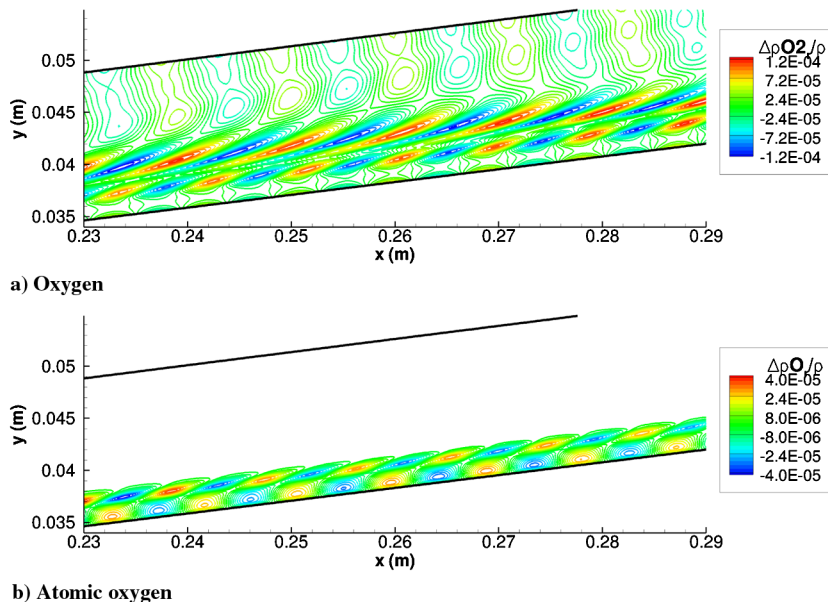


Fig. 22 Instantaneous perturbation contour plots for the 525 kHz frequency disturbance.

similar to translation-rotation temperature. For both temperatures, the maximum perturbation amplitude is the same order of magnitude.

The wave structure for oxygen and atomic oxygen is shown in an instantaneous snapshot for the 525 kHz disturbances given in Fig. 22. The second-mode wave is seen near the boundary-layer edge and is only slightly visible near the wall for oxygen. The amplitude of the second-mode wave increases in the downstream direction as the second mode becomes more dominant. For oxygen, the amplitude near the boundary-layer edge is larger than the amplitude near the wall. Freestream forcing waves are seen near the shock along with

Mach waves. In the atomic oxygen contour plot, the temperature outside of the boundary layer is not large enough for any significant amount of atomic oxygen to exist, so there are no freestream waves visible. The second-mode wave is clearly distinguishable for atomic oxygen. The magnitude of the second-mode wave is decreasing downstream for atomic oxygen because atomic oxygen is recombining to form oxygen, thus decreasing the density of atomic oxygen and its perturbation.

Since the unsteady flow is decomposed using a temporal Fourier transform, it is possible to plot the perturbation amplitudes to

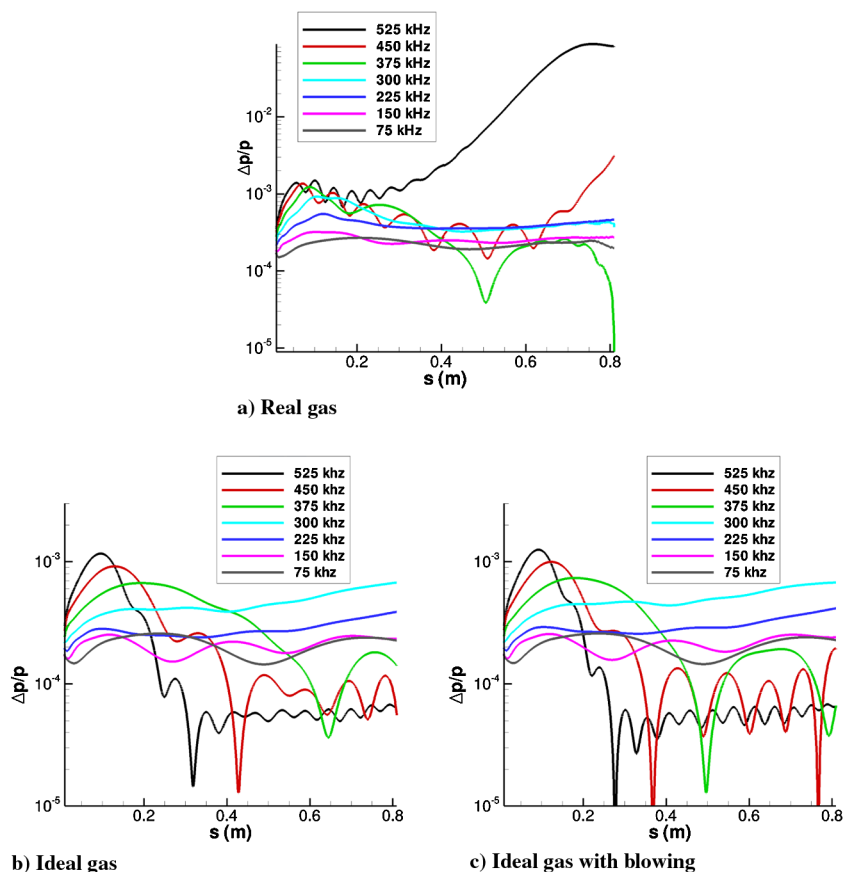


Fig. 23 Pressure perturbation amplitude at the wall computed by DNS.

determine the growth or decay of each frequency component. Figure 23 gives a comparison of the wall pressure perturbation amplitude of each frequency component for each of the three cases: real gas, ideal gas, and ideal gas with steady wall blowing. For all three cases, initial disturbance growth can be seen near $s = 0$ as a result of resonant interactions between the forcing fast-acoustic waves and the fast-acoustic mode in the boundary layer. For the real-gas case, the most unstable frequency is 525 kHz and its exponential growth starts around $x = 0.2$ m and is unstable almost to the end of the domain. This is a large unstable region of approximately 0.6 m. This growth is unstable second-mode growth. The 450 kHz disturbance becomes unstable near the end of the domain, but by this time, the disturbance flowfield has become nonlinear. It should be noted that the end of the domain (approximately $x = 0.7$ m to $x = 0.8$ m) for the real-gas simulation has surface pressure perturbation amplitudes above 1% of the freestream values. Mean flow distortion, or the zero frequency component obtained from the temporal Fourier transform, shows that velocity and pressure perturbation amplitudes at the surface near 10% of the steady base flow values at the domain exit. Also, temperature and density at the critical layer approach 1% of the freestream values at the domain exit. This significant mean flow distortion indicates that the flowfield has become nonlinear. It is possible to check for higher harmonics, which indicate flowfield nonlinearity, but the current grid is not well enough resolved to accurately capture those frequency components. As the flow becomes nonlinear, breakdown to turbulence follows, which requires a three-dimensional simulation to continue beyond $s \approx 0.8$ m.

Contrary to the real-gas case with a strong second-mode growth, the two ideal-gas cases show only minor instability. For the two ideal-gas cases, the 525 and 450 kHz disturbances exhibit no visible exponential growth downstream of $s = 0.2$ m where exponential growth was seen for the real-gas simulation. There is only some slight instability shown for the 300 and 225 kHz disturbances downstream of $x = 0.4$ m, but the growth is much smaller than the second-mode growth seen in the real-gas simulation. It is conjectured that second-mode exponential growth will start for 300 and 225 kHz further downstream, as the unstable frequency range should decrease in the streamwise direction.

The argument could be made that both ideal-gas boundary layers are stable for the chosen forcing frequencies when a different choice of forcing frequencies would lead to more marked growth. An N factor plot using ideal-gas LST is shown in Fig. 24 to address this concern. An N factor is the ratio of the integrated amplitude at a fixed physical frequency to the initial amplitude of that frequency at the neutral point. Only the ideal-gas blowing case is shown, as N factors obtained for the ideal-gas case are similar. The largest N factor over the simulated domain is 1.9 due to the 462.5 kHz second mode. The second largest N factor is 1.8 due to the 450 kHz second mode. Recall that a 450 kHz fast-acoustic wave was used as freestream forcing for each of the three DNSs. This slight difference in N factors between

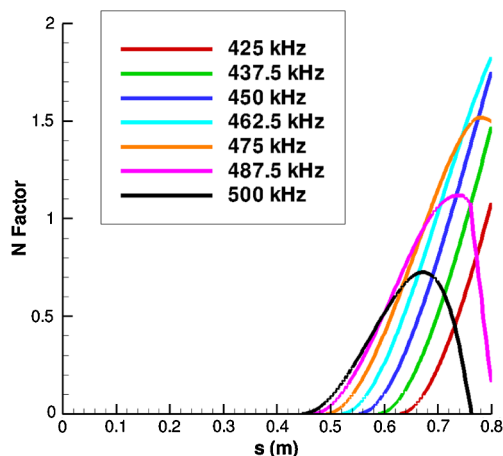


Fig. 24 Ideal-gas blowing second-mode N factor.

the most unstable frequency in the ideal-gas blowing simulation (462.5 kHz) predicted by LST and the 450 kHz freestream fast-acoustic forcing frequency would not lead to a significantly destabilized flow if different forcing frequencies had been chosen.

As the second mode is tuned to the boundary-layer thickness, the question naturally arises that differences in the unstable frequencies and their growth could be due to varying boundary-layer thicknesses between the real-gas and ideal-gas steady base flow simulations. Recall that, in Sec. VI.B, the thermal and velocity boundary-layer profiles were compared for each case and no significant difference in the boundary-layer heights existed. This rules out the possibility that the differences in boundary-layer instabilities are strongly affected by differences in boundary-layer height. The next possibility for differences in the simulations could be attributable to the steady surface blowing. As blowing rates are low (Fig. 13b) on the cone frustum and blowing is imposed for one of the ideal-gas cases, it is not likely that blowing is the main cause. If it was, the ideal-gas blowing simulation would have shown more instability. Most likely, the main cause for the large second-mode growth witnessed in the real-gas simulation is attributable to real-gas effects (chemical non-equilibrium and thermal nonequilibrium), rather than wall blowing or different boundary-layer heights. Therefore, in this case and similar high-enthalpy high-Mach-number cases, it is important to include real-gas effects when investigating boundary-layer instability and estimating transition. Further parametric study is underway to help gain a more complete understanding of these effects.

As this simulation (unlike previous DNSs of hypersonic boundary-layer instability in the open literature) accounts for graphite surface ablation, an indication of which carbon-containing species plays the largest role in second-mode instability is sought. The perturbation amplitudes for each carbon species at the wall are shown in Fig. 25. As none of the carbon species significantly diffuse away from the surface (see Fig. 15), it is difficult to visualize their perturbations except to plot them along the surface. The two most significant species amplitudes are CO and CO₂. This follows the fact that CO and CO₂ are the two carbon species that have the most mass at the wall in the steady solution, as seen in Fig. 14. It is interesting to note that the initial growth due to resonant interactions of freestream fast-acoustic waves and fast-acoustic modes seen for Δp at 525 kHz is only seen slightly in the species densities of CO and CO₂ and is not seen in the other species. This could simply be due to the fact that the mass in these species is already decreasing so quickly at the wall (Fig. 14) that the resonant interactions have little effect.

In the second-mode growth region for the 525 kHz second mode ($0.2 \text{ m} \leq s \leq 0.7 \text{ m}$), the maximum amplitudes at a single streamwise location for these two species occur at the wall, where only a slight peak is seen away from the wall. This is unlike N₂ and O₂, where there is a high amplitude near the wall and a high amplitude near the boundary-layer edge as well. This is due to the fact that CO and CO₂ are not diffusing far from the wall and have no significant mass at the boundary-layer edge. As the development of the second

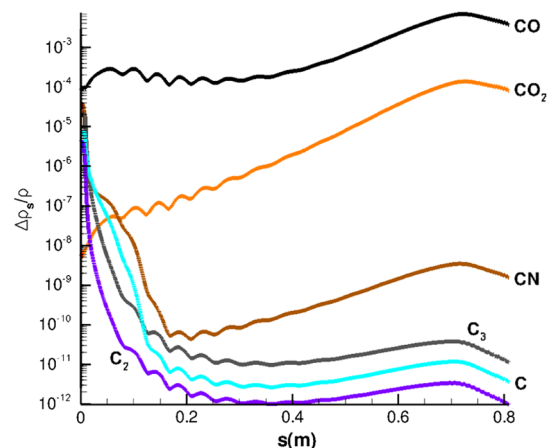


Fig. 25 Perturbation of species density for each carbon species at 525 kHz. Perturbed quantities taken at the wall and obtained from DNS.

mode strongly depends on steady flow properties near the critical layer, which moves toward the boundary-layer edge for hypersonic flows, it is possible that, in slender geometries with surface ablation where the second mode is the dominant instability mode, when blowing is small (as it is here), the effects of surface ablation on second-mode development are minimal. Note that this does not include possible ablation-induced surface roughness effects on second-mode development. Further simulations with and without surface ablation would be required to validate this argument.

VII. Conclusions

The objectives of this research are 1) to develop and validate a new high-order shock-fitting method for hypersonic flows with thermochemical nonequilibrium and graphite surface ablation, and 2) to perform an initial investigation of hypersonic boundary-layer disturbances in the presence of real-gas effects and graphite ablation effects using the developed direct numerical simulation method. An 11-species gas model without ionization is used for chemical nonequilibrium, and the two-temperature model is used for thermal nonequilibrium. The surface reactions consist of oxidation, recombination of atomic oxygen, and sublimation of C, C₂, and C₃.

Three spherical geometry cases were computed to validate the computational method. Two cases were taken from the PANT program with $M_\infty = 15.99$, where the shock-fitting results were compared to a code with similar gas and surface chemistry models. The third case was at $M_\infty = 5.84$, where the shock-fitting results were compared to a code with different gas and surface chemistry models, as well as compared to corresponding experimental data. The two PANT cases showed the shock-fitting method correctly simulated species mass concentrations in the flow as well as translation-rotation and vibration temperatures. The comparison to the third case with experimental results showed that the shock-fitting method was capable of accurately predicting surface mass flux due to graphite ablation. Overall, the new shock-fitting method compared well with established research codes.

Using the new validated high-order shock-fitting method, a direct numerical simulation was run for a 7 deg half-angle blunt cone at Mach 15.99 to find how a real-gas and graphite ablation affects boundary-layer receptivity and instability. Three separate cases were simulated in order to investigate real-gas and graphite ablation effects: real gas, ideal gas with no blowing, and ideal gas with blowing. Fast-acoustic freestream disturbances were used to perturb the steady base flow. The real-gas simulation showed a strong second-mode wave for the 525 kHz frequency. On the other hand, neither ideal-gas simulation showed significant second-mode growth for any of the simulated frequencies. Steady surface blowing was small and found to have a minimal effect for the simulated conditions. However, real-gas effects were found to significantly enhance boundary-layer instability. The results show that real-gas effects for similar flow conditions should not be ignored.

As for future work, further parametric investigation into real-gas and ablation effects on hypersonic boundary-layer stability is

required for a more complete understanding of these effects. Specifically, three-dimensional simulations should be run of blunt geometries where real-gas effects and ablative effects should have a stronger influence. Additional real-gas cases, such as simulating five-species air only, would help separate the real-gas effects due to five-species air and real-gas effects due to carbon species. Also, a thorough linear stability analysis would help to give a sound theoretical understanding of the instability physics.

Appendix A:

The various chemical reactions along with their constants (Tables A1 and A2) are listed here. Also listed here, are the viscosity coefficients (Table A3) and the sublimation constants (Table A4).

Table A2 Exchange reactions with corresponding forward reaction rate constants^a

	Reaction	$C_f, \text{m}^3/\text{mol} \cdot \text{s}$	η	θ_d, K
9	$\text{N}_2 + \text{O} \rightleftharpoons \text{NO} + \text{N}$	3.18×10^7	0.10	37,700
10	$\text{NO} + \text{O} \rightleftharpoons \text{N} + \text{O}_2$	2.16×10^2	1.29	19,220
11	$\text{CO} + \text{O} \rightleftharpoons \text{C} + \text{O}_2$	2.00×10^4	1.00	69,500
12	$\text{CN} + \text{O} \rightleftharpoons \text{NO} + \text{C}$	1.60×10^7	0.10	14,600
13	$\text{CO}_2 + \text{O} \rightleftharpoons \text{O}_2 + \text{CO}$	3.00×10^2	1.00	18,210
14	$\text{CO} + \text{C} \rightleftharpoons \text{C}_2 + \text{O}$	4.10×10^4	0.50	59,790
15	$\text{N}_2 + \text{C} \rightleftharpoons \text{CN} + \text{N}$	2.00×10^8	0.00	23,200
16	$\text{CN} + \text{C} \rightleftharpoons \text{C}_2 + \text{N}$	5.00×10^7	0.00	13,000
17	$\text{C}_3 + \text{C} \rightleftharpoons \text{C}_2 + \text{C}_2$	1.70×10^3	1.50	19,580
18	$\text{CO} + \text{N} \rightleftharpoons \text{CN} + \text{O}$	2.00×10^8	0.00	38,600
19	$\text{CO} + \text{N} \rightleftharpoons \text{NO} + \text{C}$	9.00×10^{10}	-1.00	53,200
20	$\text{CO} + \text{CO} \rightleftharpoons \text{CO}_2 + \text{C}$	1.00×10^{-3}	2.00	72,390
21	$\text{C}_2 + \text{CO} \rightleftharpoons \text{C}_3 + \text{O}$	1.20×10^7	0.00	43,240
22	$\text{CO} + \text{CO} \rightleftharpoons \text{C}_2 + \text{O}_2$	9.20×10^5	0.75	163,300
23	$\text{CO} + \text{NO} \rightleftharpoons \text{CO}_2 + \text{N}$	1.00×10^{-3}	2.00	20,980
24	$\text{N}_2 + \text{O}_2 \rightleftharpoons \text{NO} + \text{NO}$	6.69×10^3	-2.54	64,639

^aReactions 9, 10, and 24 are from Park [29]; reactions 12, 16, and 18 are from Park et al. [30]; and the remaining reactions are from Bhutta and Lewis [31].

Table A3 Species viscosity coefficients

Species	A_s^μ	B_s^μ	C_s^μ
N ₂	0.0268142	0.3177838	-11.3155513
O ₂	0.0449290	-0.0826158	-9.2019475
NO	0.0436378	-0.0335511	-9.5767430
C ₃	-0.0147000	0.8811000	-13.5051000
CO ₂	-0.0195274	1.0478180	-14.3221200
C ₂	-0.0031000	0.6920000	-12.6127000
CO	-0.0195274	1.0132950	-13.9787300
CN	-0.0025000	0.6810000	-12.4914000
N	0.0115572	0.6031679	-12.4327495
O	0.0203144	0.4294404	-11.6031403
C	-0.0001000	0.7928000	-13.4154000

Table A1 Dissociation reactions with corresponding forward reaction rate constants^a

	Reaction	Partner	$C_f, \text{m}^3/\text{mol} \cdot \text{s}$	η	θ_d, K
1	$\text{N}_2 + \text{M} \rightleftharpoons \text{N} + \text{N} + \text{M}$	All molecular species	3.70×10^{15}	-1.6	113,200
		All atomic species	1.11×10^{16}	-1.6	113,200
2	$\text{O}_2 + \text{M} \rightleftharpoons \text{O} + \text{O} + \text{M}$	All molecular species	2.75×10^{13}	-1.0	59,500
		All atomic species	8.25×10^{13}	-1.0	59,500
3	$\text{NO} + \text{M} \rightleftharpoons \text{N} + \text{O} + \text{M}$	All molecular species	2.30×10^{11}	-0.5	75,500
		All atomic species	4.60×10^{11}	-0.5	75,500
4	$\text{C}_3 + \text{M} \rightleftharpoons \text{C}_2 + \text{C} + \text{M}$	All species	1.60×10^{10}	1.0	87,480
5	$\text{CO}_2 + \text{M} \rightleftharpoons \text{CO} + \text{O} + \text{M}$	All species	1.20×10^5	0.5	36,850
6	$\text{C}_2 + \text{M} \rightleftharpoons \text{C} + \text{C} + \text{M}$	All species	4.50×10^{12}	-1.0	70,930
7	$\text{CO} + \text{M} \rightleftharpoons \text{C} + \text{O} + \text{M}$	All species	8.50×10^{13}	-1.0	129,000
8	$\text{CN} + \text{M} \rightleftharpoons \text{C} + \text{N} + \text{M}$	All species	2.50×10^8	0.0	71,000

^aReactions 1–3 are from Park [29], reaction 8 is from Park et al. [30], and reactions 4–7 are from Bhutta and Lewis [31].

Table A4 Sublimation reaction probabilities and vapor pressure coefficients^a

	α_s	P_s	Q_s
C	0.14	-85715	18.69
C ₂	0.26	-98363	22.20
C ₃	0.03	-93227	23.93

^a α_s is from Palmer [42], and P_s and Q_s are from [27].

Acknowledgments

The research was supported in part by the U.S. Air Force Office of Scientific Research/NASA National Center for Hypersonic Research in Laminar-Turbulent Transition and the U.S. Department of Defense through the National Defense Science and Engineering Graduate Fellowship Program. The computations were mainly run on Extreme Science and Engineering Discovery Environment (XSEDE) resources provided by Texas Advanced Computing Center (TACC) under grant number TG-ASC100002, supported in part by the National Science Foundation. The views and conclusions contained herein are those of the authors and should not be interpreted as necessarily representing the official policies or endorsements, either expressed or implied, of the U.S. Air Force Office of Scientific Research or the U.S. Government.

References

- [1] Ungar, E., "Ablation Thermal Protection Systems," *Science*, Vol. 158, No. 3802, 1967, pp. 740–744. doi:10.1126/science.158.3802.740
- [2] Wool, M., "Final Summary Report Passive Nosedip Technology (PANT) Program." Space and Missile Systems Organization/RSSE, SAMSO-TR-75-250, Los Angeles, June 1975.
- [3] Lin, T., "Influence of Laminar Boundary-Layer Transition on Entry Vehicle Design," *Journal of Spacecraft and Rockets*, Vol. 45, No. 2, 2008, pp. 165–175. doi:10.2514/1.30047
- [4] Keenan, J., "Thermo-Chemical Ablation of Heat Shields Under Earth Re-Entry Conditions," Ph.D. Thesis, North Carolina State Univ., Jacksonville, NC, 1994.
- [5] Zoby, E., Thompson, R., and Wurster, K., "Aeroheating Design Issues for Reusable Launch Vehicles: A Perspective," AIAA Paper 2004-2535, 2004.
- [6] Chen, Y., and Milos, F., "Navier–Stokes Solutions with Finite Rate Ablation for Planetary Mission Earth Reentries," *Journal of Spacecraft and Rockets*, Vol. 42, No. 6, 2005, pp. 961–970. doi:10.2514/1.12248
- [7] Chen, Y., and Milos, F., "Three-Dimensional Ablation and Thermal Response Simulation Sys.," AIAA Paper 2005-5064, 2005.
- [8] Lin, T., Sproul, L., and Olmos, M., "An Aerothermal Model for Ablating Heatshields," AIAA Paper 1994-0247, 1994.
- [9] Potts, R., "Application of Integral Methods to Ablation Charring Erosion. A Review," *Journal of Spacecraft and Rockets*, Vol. 32, No. 2, 1995, pp. 200–209. doi:10.2514/3.26597
- [10] Zhlukov, S., and Abe, T., "Viscous Shock-Layer Simulation of Airflow past Ablating Blunt Body with Carbon Surface," *Journal of Thermophysics and Heat Transfer*, Vol. 13, No. 1, 1999, pp. 50–59. doi:10.2514/2.6400
- [11] Park, C., "Calculation of Stagnation-Point Heating Rates Associated with Stardust Vehicle," AIAA Paper 2005-0190, 2005.
- [12] Park, C., "Effects of Atomic Oxygen on Graphite Ablation," *AIAA Journal*, Vol. 14, No. 11, 1976, pp. 1640–1642. doi:10.2514/3.7267
- [13] Mack, L., "Boundary Layer Linear Stability Theory," AGARD Rept. 709, 1984.
- [14] Malik, M., "Numerical Methods for Hypersonic Boundary Layer Stability," *Journal of Computational Physics*, Vol. 86, No. 2, 1990, pp. 376–413. doi:10.1016/0021-9991(90)90106-B
- [15] Stuckert, G., and Reed, H., "Linear Disturbances in Hypersonic, Chemically Reacting Shock Layers," *AIAA Journal*, Vol. 32, No. 7, 1994, pp. 1384–1393. doi:10.2514/3.12206
- [16] Hudson, M., Chokani, N., and Candler, G., "Linear Stability of Hypersonic Flow in Thermochemical Nonequilibrium," *AIAA Journal*, Vol. 35, No. 6, 1997, pp. 958–964. doi:10.2514/2.204
- [17] Johnson, H., Seipp, T., and Candler, G., "Numerical Study of Hypersonic Reacting Boundary Layer Transition on Cones," *Physics of Fluids*, Vol. 10, No. 10, 1998, pp. 2676–2685. doi:10.1063/1.869781
- [18] Ma, Y., and Zhong, X., "Receptivity to Freestream Disturbances of a Mach 10 Nonequilibrium Reacting Oxygen Flow over a Flat Plate," AIAA Paper 2004-0256, 2004.
- [19] Prakash, A., Parsons, N., Wang, X., and Zhong, X., "High-Order Shock-Fitting Methods for Direct Numerical Simulation of Hypersonic Flow with Chemical and Thermal Nonequilibrium," *Journal of Computational Physics*, Vol. 230, No. 23, 2011, pp. 8474–8507. doi:10.1016/j.jcp.2011.08.001
- [20] Parsons, N., Zhong, X., Kim, J., and Eldredge, J., "High-Order Shock-Fitting Methods for Hypersonic Flow with Chemical and Thermal Nonequilibrium," AIAA Paper 2010-4997, 2010.
- [21] Johnson, H., Gronvall, J., and Candler, G., "Reacting Hypersonic Boundary Layer Stability with Blowing and Suction," AIAA Paper 2009-0938, 2009.
- [22] Ghaffari, S., Marxen, O., Iaccarino, G., and Shaqfeh, E., "Numerical Simulations of Hypersonic Boundary-Layer Instability with Wall Blowing," AIAA Paper 2010-0706, 2010.
- [23] Li, F., Choudhari, M., Chang, C., and White, J., "Boundary Layer Transition over Blunt Hypersonic Vehicles Including Effects of Ablation-Induced Out-Gassing," AIAA Paper 2011-3303, 2011.
- [24] Wang, X., and Zhong, X., "A High-Order Shock-Fitting Non-Equilibrium Flow Solver for DNS of Strong Shock and Turbulence Interactions," *Seventh International Conference on Computational Fluid Dynamics*, Big Island, Hawaii, 2012.
- [25] Prakash, A., Parsons, N., Wang, X., and Zhong, X., "High-Order Shock-Fitting Methods for Hypersonic Flow with Chemical and Thermal Nonequilibrium," AIAA Paper 2010-4997, 2010.
- [26] Park, C., *Nonequilibrium Hypersonic Aerothermodynamics*, Wiley, New York, 1990, pp. 24, 57–60, 326.
- [27] Dolton, T., Maurer, R., and Goldstein, H., "Thermodynamic Performance of Carbon in Hyperthermal Environments," AIAA Paper 1968-0754, 1968.
- [28] McBride, B., Heimeil, S., Ehlers, J., and Gordon, S., "Thermodynamic Properties to 6000 for 210 Substances Involving the First 18 Elements," NASA SP-3001, 1963.
- [29] Park, C., "On Convergence of Computation of Chemically Reacting Flows," AIAA Paper 1985-0247, 1985.
- [30] Park, C., Howe, J., Jaffe, R., and Candler, G., "Chemical-Kinetic Problems of Future NASA Missions," AIAA Paper 1991-0464, 1991.
- [31] Bhutta, B., and Lewis, C., "Low-to-High Altitude Predictions of Three-Dimensional Ablative Reentry Flowfields," AIAA Paper 1992-0366, 1992.
- [32] Lee, J., "Basic Governing Equations for the Flight Regimes of Aeroassisted Orbital Transfer Vehicles," *Thermal Design of Aeroassisted Orbital Transfer Vehicles*, edited by Nelson, H. F., Vol. 96, AIAA, New York, 1985, pp. 3–53.
- [33] Millikan, R., and White, D., "Systematics of Vibrational Relaxation," *Journal of Chemical Physics*, Vol. 39, No. 12, 1963, pp. 3209–3213. doi:10.1063/1.1734182
- [34] Blottner, F., Johnson, M., and Ellis, M., "Chemically Reacting Gas Viscous Flow Program for Multi-Component Gas Mixtures," Sandia National Labs. Rept. SC-RR-70-754, Albuquerque, NM, 1971.
- [35] Gupta, R., Lee, K., and Sutton, K., "Viscous-Shock-Layer Solutions with Coupled Radiation and Ablation Injection for Earth Entry," AIAA Paper 1990-1697, 1990.
- [36] Candler, G., "Computation of Thermo-Chemical Nonequilibrium Martian Atmospheric Entry Flow," AIAA Paper 1990-1695, 1990.
- [37] Wilke, C., "A Viscosity Equation for Gas Mixtures," *Journal of Chemical Physics*, Vol. 18, No. 4, 1950, pp. 517–519. doi:10.1063/1.1747673
- [38] Zhong, X., "High-Order Finite-Difference Schemes for Numerical Simulation of Hypersonic Boundary-Layer Transition," *Journal of Computational Physics*, Vol. 144, No. 2, 1998, pp. 662–709. doi:10.1006/jcp.1998.6010
- [39] Suzuki, T., Fujita, K., Ando, K., and Sakai, T., "Experimental Study of Graphite Ablation in Nitrogen Flow," *Journal of Thermophysics and Heat Transfer*, Vol. 22, No. 3, 2008, pp. 382–389. doi:10.2514/1.35082
- [40] Park, C., and Bogdanoff, D., "Shock-Tube Measurements of Nitridation Coefficient of Solid Carbon," *Journal of Thermophysics and Heat*

- Transfer*, Vol. 20, No. 3, 2006, pp. 487–492.
doi:10.2514/1.15743
- [41] Baker, R., “Graphite Sublimation Chemistry Nonequilibrium Effects,” *AIAA Journal*, Vol. 15, No. 10, 1977, pp. 1391–1397.
doi:10.2514/3.60806
- [42] Palmer, H., and Mordecia, S., *Chemistry and Physics of Carbon*, Marcel Dekker, New York, 1968, p. 126.
- [43] Park, C., “Stagnation-Point Ablation of Carbonaceous Flat Disks, Part 1: Theory,” *AIAA Journal*, Vol. 21, No. 11, 1983, pp. 1588–1594.
doi:10.2514/3.8293
- [44] Park, C., “Review of Chemical-Kinetic Problems of Future NASA Missions, 1: Earth Entries,” *Journal of Thermophysics and Heat Transfer*, Vol. 7, No. 3, 1991, pp. 385–398.
doi:10.2514/3.431
- [45] Saric, W., Reed, H., and Kerschen, E., “Boundary-Layer Receptivity to Freestream Disturbances,” *Annual Review of Fluid Mechanics*, Vol. 34, Jan. 2002, pp. 291–319.
doi:10.1146/annurev.fluid.34.082701.161921
- [46] Fedorov, A., “Transition and Stability of High-Speed Boundary Layers,” *Annual Review of Fluid Mechanics*, Vol. 43, Jan. 2011, pp. 79–95.
doi:10.1146/annurev-fluid-122109-160750
- [47] Zhong, X., and Wang, X., “Direct Numerical Simulation on the Receptivity, Instability, and Transition of Hypersonic Boundary Layers,” *Annual Review of Fluid Mechanics*, Vol. 44, Jan. 2012, pp. 527–561.
doi:10.1146/annurev-fluid-120710-101208
- [48] Stetson, K., Thompson, E., Donaldson, J., and Siler, L., “Laminar Boundary Layer Stability Experiments on a Cone at Mach 8, Part 2: Blunt Cone,” AIAA Paper 1984-0006, 1984.
- [49] Ma, Y., and Zhong, X., “Receptivity of a Supersonic Boundary Layer over a Flat Plate, Part 1. Wave Structures and Interactions,” *Journal of Fluid Mechanics*, Vol. 488, July 2003, pp. 31–78.
doi:10.1017/S0022112003004798
- [50] Mortensen, C., and Zhong, X., “Real Gas and Surface Ablation Effects on Hypersonic Boundary Layer Instability over a Blunt Cone,” AIAA Paper 2013-2981, 2013.
- [51] Tumin, A., “Multimode Decomposition of Spatially Growing Perturbations in a Two-Dimensional Boundary Layer,” *Physics of Fluids*, Vol. 15, No. 9, 2003, p. 2525.
doi:10.1063/1.1597453

M. Choudhari
Associate Editor